

THE MILLIMETER ASTRONOMY LEGACY TEAM 90 GHZ (MALT90) PILOT SURVEY

JONATHAN B. FOSTER¹, JAMES M. JACKSON¹, ELIZABETH BARRIS¹, KATE BROOKS², MARIA CUNNINGHAM³, SUSANNA C. FINN¹, GARY A. FULLER⁴, STEVE N. LONGMORE^{5,6}, JOSHUA L. MASCOOP¹, NICOLAS PERETTO⁷, JILL RATHBORNE^{2,8}, PATRICIO SANHUEZA¹, FRÉDÉRIC SCHULLER⁹, FRIEDRICH WYROWSKI⁹

Draft version April 17, 2018

ABSTRACT

We describe a pilot survey conducted with the Mopra 22-m radio telescope in preparation for the Millimeter Astronomy Legacy Team Survey at 90 GHz (MALT90). We identified 182 candidate dense molecular clumps using six different selection criteria and mapped each source simultaneously in 16 different lines near 90 GHz. We present a summary of the data and describe how the results of the pilot survey shaped the design of the larger MALT90 survey. We motivate our selection of target sources for the main survey based on the pilot detection rates and demonstrate the value of mapping in multiple lines simultaneously at high spectral resolution.

Subject headings: ISM: molecules — stars: massive — stars: formation — surveys

1. INTRODUCTION

The goal of the Millimeter Astronomy Legacy Team Survey at 90 GHz (MALT90) is to characterize the physical and chemical conditions of dense molecular clumps associated with high-mass star formation over a wide range of evolutionary states. MALT90 will do this by taking advantage of the newly upgraded Mopra Spectrometer (MOPS¹) and the fast mapping capability of the Mopra 22-m radio telescope². The survey will obtain molecular line maps of 3000 candidate dense molecular clumps. The clumps will be selected so as to cover a broad range of evolutionary states, from pre-stellar clumps to accreting high-mass protostars and on to H II regions. The survey will be conducted at 90 GHz because this frequency regime contains numerous molecular lines which have typical critical densities for collisional excitation of $\gtrsim 10^5 \text{ cm}^{-3}$ and are therefore excellent tracers of dense gas. Such data will allow us to study the Galactic distribution of these clumps, their physical properties, and their chemical variation and evolution; this basic information is necessary to constrain theories of high-mass star formation. In addition, MALT90 will provide a valuable database of dense molecular clumps associated with high-mass star formation for future ALMA observations.

MALT90 will map roughly 3,000 dense molecular clumps, providing an order of magnitude more sources than previous comparable surveys (e.g., Shirley et al. 2003; Pirogov et al. 2003; Gibson et al. 2009; Wu et al. 2010). A large number of sources will allow us to divide the sample into sub-samples (based on mass, evolutionary phase, etc.) yet retain a sufficient number of sources in each sub-sample for statistical analysis. Because dense molecular gas occupies only a small solid angle of the Galactic plane and molecular emission at 90 GHz is relatively faint, a blind fully-sampled 90 GHz survey of a significant portion of the Galactic plane is impractical. Instead, we must choose targets based on other methods for identifying dense molecular clumps. The main purpose of the MALT90 pilot survey described herein is to choose the best method for identifying dense molecular clumps, with the twin aims of having a high percentage of detections within our sensitivity limits and covering a broad range of evolutionary states.

Throughout this paper, we will use the term “dense molecular clump” to refer to our sources. The choice of “clump” follows the naming system used by Williams et al. (2000) and Bergin & Tafalla (2007) which distinguishes between molecular clouds, clumps, and cores. In this scheme, clumps are coherent regions in position-velocity space with typical masses of 50-500 M_{\odot} , typical sizes of 0.3-3 pc and typical mean densities of 10^3 - 10^4 cm^{-3} which may contain additional substructures called cores which give rise to individual stars or stellar systems. Our goal in MALT90 is to identify and map the clumps that give rise to a cluster of stars containing one or more high-mass stars.

This paper will focus predominantly on the technical validation of the survey and explain the design choices motivated by the pilot survey. Data from the pilot survey will be combined with the full MALT90 survey data (where the diverse selection criteria in the pilot survey are not detrimental to statistical analysis) for the specific scientific projects in MALT90. These analyses will appear in future papers.

¹ MOPS was funded in part through a grant instigated by the University of New South Wales (UNSW) under the Australian Re-

jbfoster@bu.edu

¹ Institute for Astrophysical Research, Boston University, Boston, MA 02215, USA

² CSIRO Astronomy and Space Science, PO Box 76, Epping, NSW 1710, Australia

³ School of Physics, The University of New South Wales, Sydney 2052, Australia

⁴ Jodrell Bank Centre for Astrophysics, School of Physics and Astronomy, University of Manchester, Manchester M13 9PL, UK

⁵ ESO Headquarters, Karl-Schwarzschild-Str. 2, 85748 Garching bei München, Germany

⁶ Harvard-Smithsonian Center for Astrophysics, MS 42, 60 Garden Street, Cambridge, MA 02138, USA

⁷ Laboratoire AIM, CEA/DSM-CNRS-Université Paris Diderot, IRFU/Service d'Astrophysique, C.E. Saclay, Orme de Merisiers, 91191 Gif-sur-Yvette, France

⁸ Departamento de Astronomía, Universidad de Chile, Chile

⁹ Max-Planck-Institut für Radioastronomie, Auf dem Hügel 69, D-53121 Bonn, Germany

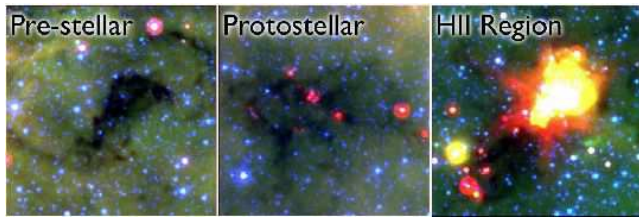


Figure 1. A proposed evolutionary sequence for high-mass star formation, running from pre-stellar clumps [left], to clumps with embedded accreting protostars [middle], to H II regions [right]. These three-color images show IRAC band 1 ($3.6 \mu\text{m}$) as blue, IRAC band 4 ($8.0 \mu\text{m}$) as green, and MIPS $24 \mu\text{m}$ as red. These categories correspond to different *Spitzer* emission morphologies and motivated the three different catalogs based on GLIMPSE and MIPS GAL data. Specifically, clumps which are dark at GLIMPSE wavelengths ($3.6 - 8 \mu\text{m}$) are identified as pre-stellar, clumps with a MIPS GAL $24 \mu\text{m}$ point source are identified as protostellar, and clumps with extended $8 \mu\text{m}$ flux are identified as H II regions.

2. TARGET SELECTION

We used six different input catalogues for selecting sources; three were lists that we produced for our pilot survey and three were based on pre-existing catalogs. From these lists we chose 20 - 40 sources near integer Galactic longitudes covering the range of longitudes accessible from Mopra. This assured a random selection of sources from the three pre-compiled lists and allowed us to focus on a limited portion of the sky when developing our own lists, while still covering a broad range of Galactic longitudes. The six selection criteria are summarized in Table 1.

The first three lists were produced for our pilot survey. For these lists we chose sources based on the mid-infrared morphology of candidate dense molecular clumps as revealed by two *Spitzer* Space Telescope Legacy surveys: the Galactic Legacy Infrared Mid-Plane Survey Extraordinaire (GLIMPSE; Benjamin et al. 2003) and the 24 and 70 Micron Survey of the Inner Galactic Disk with MIPS (MIPSGAL; Carey et al. 2009). GLIMPSE covers the Galactic plane in the Infrared Array Camera (IRAC; Fazio et al. 2004) bands from 3.6 to $8.0 \mu\text{m}$, while MIPSGAL covers much the same area at 24 and $70 \mu\text{m}$ using the Multiband Infrared Photometer for *Spitzer* (MIPS; Rieke et al. 2004).

We examined the GLIMPSE and MIPSGAL mosaics using three criteria designed to select sources in distinct evolutionary states as shown in Figure 1. A preliminary version of the Peretto & Fuller (2009) catalog of Infrared Dark Clouds (IRDCs) was used to identify $8 \mu\text{m}$ extinction features near integer Galactic longitudes. This catalog was then trimmed to remove any sources which contained a $24 \mu\text{m}$ point source (since this is most likely a protostar). We refer to this the GLIMPSE-Dark catalog, and these sources should correspond to the earliest phase of high-mass star formation. We then examined the *Spitzer* mosaics near integer Galactic longitudes by hand to choose candidate dense molecular clumps containing either $24 \mu\text{m}$ point sources or bright extended $8 \mu\text{m}$ emission. If a clump of $8 \mu\text{m}$ dark extinction was co-

incident with a $24 \mu\text{m}$ point source, we assigned it to the MIPSGAL catalog and classified this candidate clump as protostellar. In the case of bright extended emission at $8 \mu\text{m}$ we assigned the source to the GLIMPSE-Bright catalog and classified it as an H II region.

The correspondence between the appearance of a source in the *Spitzer* surveys and its evolutionary state is clearly imperfect. The projection of unrelated objects along a given line of sight, inhomogeneities in the diffuse $8 \mu\text{m}$ emission, and sensitivity limits (e.g., our ability to detect $24 \mu\text{m}$ point sources will depend on intrinsic luminosity and distance) are three possible sources of misidentification. However, this system provides a quick and uniform way to make an initial assessment of a candidate dense molecular clump's evolutionary state.

The other three lists in our pilot survey were produced using pre-existing catalogs. The first came from the H₂O Southern Galactic Plane Survey (HOPS; Walsh et al. 2008) which used Mopra at 1.2 cm to map the Galactic plane from $-70^\circ < l < 30^\circ$ in NH₃ and H₂O. Because the HOPS NH₃ (1,1) and (2,2) lines have a similar critical density ($n \sim 10^4 \text{ cm}^{-3}$) as the MALT90 90 GHz lines ($n \sim 10^5 \text{ cm}^{-3}$), bright NH₃ sources in HOPS are likely to be detected by Mopra in the 90 GHz lines. The last two catalogs came from mm/submm continuum surveys which reveal the location of regions with high dust column density, typically corresponding to dense molecular clumps. The Beltrán et al. (2006) survey at 1.2 mm made maps around Infrared Astronomical Satellite (IRAS) point sources using the Swedish-ESO SubMillimeter Telescope (SEST) and the SEST Imaging Bolometer Array (SIMBA). Because the Beltrán et al. (2006) maps were made toward IRAS point sources, these sources are likely to contain a protostar or H II region, which gives rise to the IRAS emission; we shall refer to this catalog as the IRAS catalog for convenience. Finally, the APEX (Atacama Pathfinder Experiment) Telescope Large Area Survey of the Galaxy (ATLASGAL; Schuller et al. 2009) is a survey of the Galactic plane ($\pm 60^\circ$ in longitude over $\pm 1.5^\circ$ in latitude and $-80^\circ \leq l \leq -60^\circ$ with $-2^\circ \leq b \leq 1^\circ$) at $870 \mu\text{m}$. From a preliminary compact source catalog we chose ATLASGAL sources with peak fluxes above 2 Jy/beam closest to integer Galactic longitudes.

In two cases (G336.994-00.019 and G339.968-00.529), a candidate dense molecular clump was chosen independently from two different catalogs. We consider these sources to belong to both catalogs when considering detection statistics.

In summary, we have combined six separate lists, four of which we expected to select particular evolutionary states (the *Spitzer*-identified sources and the Beltrán et al. (2006) catalog of IRAS sources), and two of which (ATLASGAL and HOPS) we expected to be less biased with respect to evolutionary status. For both ATLASGAL and HOPS, the most luminous sources will tend to be the hottest, more evolved sources. To select a broad range of evolutionary states from these surveys it is necessary to include some additional information as we discuss in § 5.2.

3. DATA

We carried out observations for the MALT90 pilot survey in the austral winter of 2009 from June 15-24. The

search Council Grants scheme for Linkage, Infrastructure, Equipment and Facilities (LIEF), and in part by CSIRO Astronomy and Space Science.

² The Mopra radio telescope is part of the Australia Telescope National Facility which is funded by the Commonwealth of Australia for operation as a National Facility managed by CSIRO.

Table 1
MALT90 Pilot Survey Input Catalogs

Data	Criterion	Object Identified	Shorthand
GLIMPSE 3.6 to 8 μm	Dark Extinction	Pre-stellar (IRDC) Clump	GLIMPSE-Dark
GLIMPSE 8 μm	Extended Emission	H II Region	GLIMPSE-Bright
MIPSGAL 24 μm	Point Source	Accreting Protostar	MIPSGAL
HOPS ^a 1.2 cm	Compact NH ₃ Source	Dense Clump	HOPS
IRAS + 1.2 mm emission ^b	IRAS + mm Continuum	Star-forming Dense Clump	IRAS
ATLASGAL ^c 870 μm	Compact Continuum	Dense Clump	ATLASGAL

^a Walsh et al. (2008)

^b Beltrán et al. (2006)

^c Schuller et al. (2009)

On-The-Fly (OTF) mapping mode of Mopra was used. Maps were made with the beam center running on a $3'.4 \times 3'.4$ grid. At typical distances to high-mass star-forming regions (several kpc) this map size is sufficient to cover the expected spatial extent of a few parsecs for our dense molecular clumps. The scan rate was $3.92''$ per second. The map is made with $12''$ spacing between the rows, giving 17 rows per map. Since the Mopra beam at 90 GHz is $36''$, this row spacing provides redundancy in the map. OFF positions were chosen at ± 1 degree in Galactic latitude away from the plane (positive offset for sources at positive Galactic latitude and vice-versa), and though the OFF positions were not explicitly checked for line emission, no map showed evidence of contamination from signal in the OFF. A single OFF position was observed for every two scan rows. In general, maps were made scanning in strips of constant Galactic longitude, although for two sources maps were also taken by scanning in strips of constant Galactic latitude.

Pointing on SiO masers was performed every 1-1.5 hour, maintaining pointing precision to better than about $10''$. Typical system temperatures (T_{sys}) were 150 - 250 K and were measured by paddle scans every 15 minutes. Weather conditions were variable. Sources observed under poor system temperatures ($T_{\text{sys}} > 500$ K) or rapidly varying conditions were re-observed under more clement conditions. For each source, only the map taken with the lowest T_{sys} is presented here.

The full 8 GHz bandwidth of MOPS was split into 16 zoom bands of 138 MHz each providing a velocity resolution of $\sim 0.11 \text{ km s}^{-1}$ in each band, easily sufficient to resolve line emission in a high-mass star-forming region. The central frequencies are shown in Table 2, along with the line targeted at that frequency and what information that line primarily provides. The strongest lines were $\text{N}_2\text{H}^+(1-0)$, $\text{HNC}(1-0)$, $\text{HCO}^+(1-0)$, and $\text{HCN}(1-0)$. These lines are all good tracers of dense gas, but provide slightly different information. N_2H^+ is more resistant to freeze-out on grains than the carbon-bearing species (Bergin et al. 2001). HNC is particularly prevalent in cold gas (Hirota et al. 1998). HCO^+ often shows infall signatures and outflow wings (e.g., Rawlings et al. 2004; Fuller et al. 2005). These strong lines can all be optically thick. Two isotopologues, $\text{H}^{13}\text{CO}^+(1-0)$ and $\text{H}^{13}\text{CN}(1-0)$ were also observed and provide optical depth and line profile information. $^{13}\text{CS}(2-1)$ is another optically thin column density tracer by virtue of its low abundance. We also include $^{13}\text{C}^{34}\text{S}(2-1)$ but this molecule is too rare to be detected.

A number of lines were chosen as tracers of hot core chemistry: $\text{CH}_3\text{CN}(J_K = 5_1 - 4_1)$, $\text{HC}_3\text{N}(J = 10 - 9)$, $\text{HC}^{13}\text{CCN}(J = 10 - 9, F = 9 - 8)$, $\text{HNCO}(J_{K_a, K_b} = 4_{0,4} - 3_{0,3})$, $\text{HNCO}(J_{K_a, K_b} = 4_{1,3} - 3_{1,2})$ (Brown et al. 1988). These carbon-bearing species are typically only seen in the hot cores around high-mass protostars once molecules have been liberated off dust grains by radiation or shocks. Three more lines trace particular environments: the recombination line $\text{H}41\alpha$ traces ionized gas (Shukla et al. 2004); $\text{SiO}(2-1)$ is seen when SiO is formed from shocked dust grains, typically in outflows (Schilke et al. 1997); C_2H is produced in photodissociation regions (e.g., Lo et al. 2009; Gerin et al. 2011), the $N = 1 - 0, J = 3/2 - 1/2, F = 2 - 1$ transition is the strongest of several C_2H lines in this spectral window. Henceforth we will refer to these line transitions by the molecule name where this usage is unambiguous (i.e. HCO^+ instead of $\text{HCO}^+(1-0)$).

The maps were reduced using the LIVEDATA and GRIDZILLA packages¹⁰. LIVEDATA performs bandpass calibration using reference OFF scans and fits a 2nd order polynomial to the baseline. GRIDZILLA uses this output to construct a uniformly gridded cube. Both polarizations were averaged together. A top-hat smoothing kernel with radius of $30''$ was used to determine which spectra contribute signal to a pixel in the output map, and spectra were weighted by the system temperature. This choice of parameters produces an effective beam size of $\text{FWHM} = 72''$. The final cube is over-sampled in spatial frequency ($9''$ pixels) and is $4'.6 \times 4'.6$ with the edges having significantly lower coverage, i.e. integration time. The data are presented on the antenna temperature scale (T_A^*). The beam efficiency of Mopra is between 0.49 at 86 GHz and 0.42 at 115 GHz (Ladd et al. 2005) for converting T_A^* into main-beam brightness temperature (T_{mb}). All the data are publicly available from the MALT90 website¹¹.

4. ANALYSIS

The MALT90 pilot survey data were used to test some of the analysis tools in development for the full survey. Three different methods were used to assess detection statistics: (1) “by-hand” examination, (2) automated Gaussian fitting based on the HOPS (Walsh et al. 2008) pipeline and (3) moment maps. Although Gaussian fitting is critical for certain measurements (particularly for lines with hyperfine component), moment maps are a fast

¹⁰ <https://www.atnf.csiro.au/people/mcalabre/livedata.html>

¹¹ <http://malt90.bu.edu>

Table 2
MALT90 Pilot Survey Lines

IF	Species	Transition	ν_0 (GHz)	Primary Information Provided
1	N ₂ H ⁺	$J = 1 - 0$	93.173772	High column density, depletion resistant, optical depth
2	¹³ CS	$J = 2 - 1$	92.494303	High column density
3	H	41 α	92.034475	Ionized gas
4	CH ₃ CN	$J_K = 5_1 - 4_1$	90.979020	Hot core
5	HC ₃ N	$J = 10 - 9$	91.199796	Hot core
6	¹³ C ³⁴ S	$J = 2 - 1$	90.926036	High column density
7	HNC	$J = 1 - 0$	90.663572	High column density, cold gas
8	HC ¹³ CCN	$J = 10 - 9, F = 9 - 8$	90.593059	Hot core
9	HCO ⁺	$J = 1 - 0$	89.188526	High column density, kinematics
10	HCN	$J = 1 - 0$	88.631847	High column density, optical depth
11	HNCO	$J_{K_a, K_b} = 4_{0,4} - 3_{0,3}$	88.239027	Hot core
12	HNCO	$J_{K_a, K_b} = 4_{1,3} - 3_{1,2}$	87.925238	Hot core
13	C ₂ H	$N = 1 - 0, J = 3/2 - 1/2, F = 2 - 1$	87.316925	Photodissociation region
14	SiO	$J = 2 - 1$	86.847010	Shock/outflow
15	H ¹³ CO ⁺	$J = 1 - 0$	86.754330	High column density, optical depth
16	H ¹³ CN	$J = 1 - 0$	86.340167	High column density, optical depth

Note. — Frequencies listed above are the rest frequencies used in converting to velocity scale (FITS keyword RESTFREQ).

and relatively robust way to measure basic line properties and this study will focus only on properties well-measured by moment analysis. The results of the “by-hand” examination were used to select the parameters used in generating moment maps.

As a first step to making moment maps, we calculated an error map for each spatial pixel by computing the standard deviation of the spectra at that position using 3σ iterative rejection. In this way, we remove strong line features from the calculation and derive an estimate of the per-channel noise in the spectrum at each point in the map. Our on-the-fly maps have less integration time at the edges, so a spatial error map is required in order to properly assess features near the noisy edges of the map.

Zeroth (M_0 ; integrated intensity), first (M_1 ; central velocity), and second (M_2 ; line-width) moment maps were made according to

$$M_0 = \int I(\nu) d\nu \quad (1)$$

$$M_1 = \frac{1}{M_0} \int I(\nu) \nu d\nu \quad (2)$$

$$M_2 = \sqrt{\frac{1}{M_0} \int I(\nu) (\nu - M_1)^2 d\nu} \quad (3)$$

where $I(\nu)$ is the intensity at a given frequency, ν . The error on the zeroth moment is simply

$$\sigma_{M_0} = \sigma \sqrt{n} \quad (4)$$

where σ is the per-channel noise in the spectrum as calculated for our error map and n is the number of spectral channels used. Errors on the first and second moment (σ_{M_1} and σ_{M_2}) are calculated from propagation of uncertainty on the formulae for M_1 and M_2 above, but are omitted for space.

The main choice in making moment maps lies in identifying the region of the cube to use. For the pilot survey automatic line detection was hindered by baseline ripples (particularly in worse weather) and noisy edges on the bandpasses. Improvement to the data processing

pipeline are expected to mitigate baseline ripples for the full MALT90 survey and allow for automatic detection of lines, but these were not available for processing the pilot data. Therefore we use hand-identified velocities for each source to make moment maps in fixed-width windows around these velocities. Hand-identified velocities were estimated by recording the velocity at the center of each line as estimated by eye and averaging the velocities from whichever of the four main lines (N₂H⁺, HNC, HCO⁺, HCN) were clearly detected above the noise. Where no line could be identified (53 sources), no moment map was made.

Two different velocity ranges were used for making moment maps, a narrow range for detection and a broader range for measuring line properties. A narrow velocity range (± 2.25 km s⁻¹) produced the highest signal to noise measurement for weak, narrow lines by limiting the spectral region considered to the peak of the line. Typical full-width at half-maxima line-widths (ΔV_{FWHM}) for our sources are between 5 and 8 km s⁻¹ (as measured in HNC; see § 5.1), so this narrow velocity range does not adequately measure line properties. Therefore, a broader velocity range (± 8.25 km s⁻¹) was also used to make moment maps. This range typically covers most of the line down to the noise, and thus comes much closer to estimating the true moments of the line. In addition, it includes the hyperfine components in both the N₂H⁺ and HCN lines, providing a better measure of the integrated intensity for those lines; the trade-off is higher noise. We therefore report detections from the narrow velocity integration range (± 2.25 km s⁻¹) and report moment information from the broader range (± 8.25 km s⁻¹).

Integrated intensity (M_0) maps for each source detected in any line are presented in Figure Set 2. To facilitate inter-comparison, all maps are displayed on the same intensity scale, with the lowest contour at 1 K km s⁻¹ which is a typical 5σ uncertainty in the integrated intensity. These moment maps are all made in a fixed velocity range around hand-identified central velocities. We show the spectra for our four main lines at their respective positions of maximum integrated intensity in

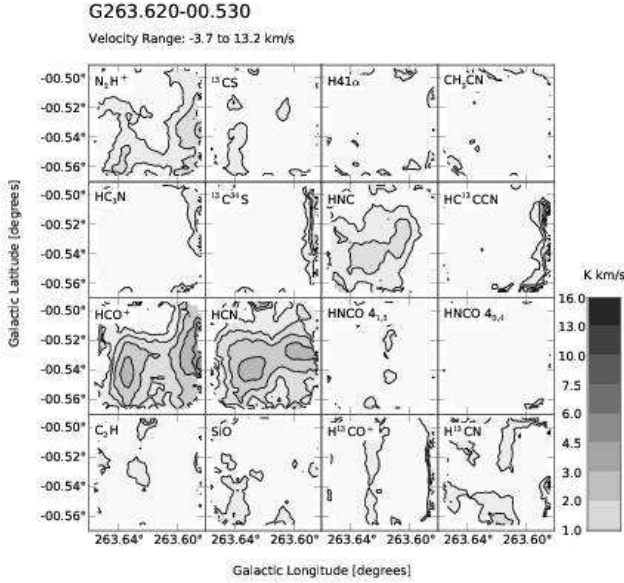


Figure 2. Example integrated intensity (zeroth moment; M_0) map of G263.620–00.530. A uniform color-scale is used in all figures in this figure-set, starting at 1 K km s^{-1} which is a typical $5\sigma_{m_0}$ contour for our dataset. Maps taken in worse weather have higher noise and the edges of the maps have higher noise, so not all emission at this level is necessarily significant. We use spatially varying noise maps to identify genuinely significant emission for the analysis presented in the text. Figure 1 of 134 in this figureset.

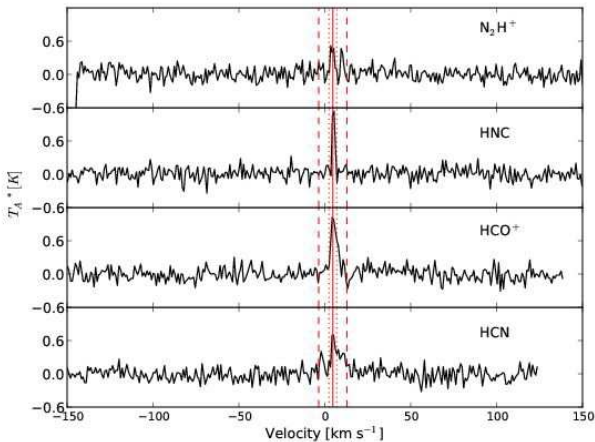


Figure 3. Spectra of our four main lines at their respective positions of maximum integrated intensity (or in the center of the map for non-detections) for G263.620–00.530. Vertical [red] lines show the central velocity estimated by hand [solid], the small velocity range used for detection [dotted line], and larger velocity range used for measuring moments [dashed line]. Figure 1 of 182 in this figureset.

Figure Set 3. For sources without any detections Figure Set 3 shows the spectra at the center of the map.

Basic source properties, including our hand-determined centroid velocities and the per-channel standard deviation at the center of the map (which is representative of the fully-sampled portion of the map) are summarized in Table 3. In five cases, two distinct

and widely separated velocity components were seen in a source. In these cases, each velocity component was used to create moment maps. The stronger line is listed first in Table 3 and is the main line used when considering detection statistics. We did not consider these as separate sources for the detection statistics (because we are interested in knowing if a given catalog will give us a detection at a given spatial position), but did consider them as separate sources (giving us a total of 187 sources) when considering the distributions of measured moments (because they are likely two separate dense molecular clumps at distinct distances as well as velocities).

The positions of maximum integrated intensity within each map were found by making a signal-to-noise ratio map from M_0 and σ_{M_0} , setting the poorly-sampled three edge pixels to zero, boxcar smoothing by a factor of three (i.e. taking the sliding average of three pixels), and identifying the maximum value. This process produces a potentially different maximum integrated intensity position for each line, but this is desirable as several of our sources exhibit strong spatial variation in line intensity ratios. The parameters of the four main lines (N_2H^+ , HNC, HCO^+ , HCN) at their respective positions of maximum integrated intensity are listed in Table 4.

5. RESULTS

5.1. Detection Statistics and Line Properties

The large size of our data set requires that we set a high level of significance when searching for features to avoid many false positives. With 187 sources, each with 16 lines and 31×31 pixels in each map we are searching for line detections in nearly 3 million spectra. A 5σ detection criteria should produce one false positive per 1.7 million measurements (for a perfectly normal distribution). We consider this to be an acceptably small level of contamination, and refer to a 5σ detection as a robust detection. Additional selection criteria combined with a lower detection threshold could be used to search for additional weak lines. For instance, to improve the completeness of H^{13}CO^+ detections we could adopt a lower σ threshold while constraining the search to locations with significant HCO^+ flux.

Our robust detection rates of the four main lines (N_2H^+ , HNC, HCO^+ , and HCN) were high ($> 90\%$) for the HOPS, ATLASGAL and IRAS catalogs, and lower ($< 60\%$) for sources chosen based on the morphology of *Spitzer* emission (see Figure 4). Detection rates were comparable for the HOPS, ATLASGAL and IRAS samples, and similar for all four species. Five additional species had robust detections: C_2H , ^{13}CS , SiO, H^{13}CO^+ and H^{13}CN . These detection rates are presented in Figure 5. C_2H , in particular, was commonly seen, with detection rates between 10 and 90% for the six different surveys. Again, the HOPS, ATLASGAL and IRAS catalogs produced more robust detections than the catalogs based on the morphology of *Spitzer* emission. The low detection rates of the three input catalogs based on *Spitzer* morphology are likely due to these catalogs identifying features which are not truly associated with dense clumps. For instance, 10% to 20% of the IRDC candidates in the Peretto & Fuller (2009) catalog are not detected in the Herschel Hi-GAL survey

(Peretto et al. 2010) and only 58% of the IRDC candidates in the Simon et al. (2006) catalog are detected in CS (Jackson et al. 2008). These non-detections suggest that the IRDC catalogs contain sources with a range of column densities, including sources with low column densities that do not have sufficient column density to be observed with the sensitivity limits of this survey. Table 5 presents the detections and non-detections of lines for all the sources.

The detection statistics correspond to the brightest integrated emission anywhere in the map, not necessarily at the center of the map. Each input catalog provides a central position of the source, which was used as the center of the map. The positions of maximum integrated intensity tend to be clustered at the center of our images (see Figure 6) with 50% of maximum integrated intensity detections for each of the four main lines occurring within $40''$ of the map center. This suggests that the input catalog positions are good choices for the center of the map.

The observed distributions of the integrated intensities and line-widths of the four main species (N_2H^+ , HNC, HCO^+ , and HCN) at the brightest point in each map are displayed in Figures 7 and 8. Again, the detection criteria is $M_0 > 5\sigma$ in the narrow ($\pm 2.25 \text{ km s}^{-1}$) integration range, but the integrated intensities shown in Figures 7 and 8 and reported in Table 4 are based on the broader range ($\pm 8.25 \text{ km s}^{-1}$); some lines are no longer 5σ measurements when using the broader velocity integration range.

The integrated intensities for the four main species at their brightest location in each map show broadly similar distributions. All are incomplete below 2 K km s^{-1} due to our noise and detection level. Two sources have extremely bright and broad HCO^+ lines, with $M_0 > 20 \text{ K km s}^{-1}$, possibly indicating the presence of outflows. HNC has relatively fewer lines which are both broad and bright. Although integrated intensity is a distance-dependent measurement, most sources are detected in all four lines at the same velocity (and thus distance) or in none of these lines. Therefore the similarity of integrated intensity distributions shows that the line luminosity distributions for these transitions are similar for the majority of these sources (see § 5.3.1 for some counter-examples).

We calculate an effective ΔV_{FWHM} from the second moment (M_2) with the formula for a Gaussian profile ($\Delta V_{\text{FWHM}} = \sqrt{8 \ln 2} \times M_2$), despite the fact that many lines deviate from a Gaussian profile. ΔV_{FWHM} are often reported as a proxy for second moment, so we report this effective ΔV_{FWHM} to facilitate comparison with other studies. We report this quantity only for HNC and HCO^+ . N_2H^+ and HCN are excluded because their hyperfine structure prohibits making a line-width measurement solely from our moment maps.

We compare the HCO^+ and HNC line-width distributions in Figure 8 for sources where $M_2/\sigma_{M_2} > 3$. We break down the HCO^+ distribution based on whether H^{13}CO^+ is detected for a given source. The detection of this rare isotope typically indicates an optically thick HCO^+ line (although a non-detection of H^{13}CO^+ is not a guarantee that HCO^+ is optically thin). The distributions of ΔV_{FWHM} for HCO^+ and HNC are broadly

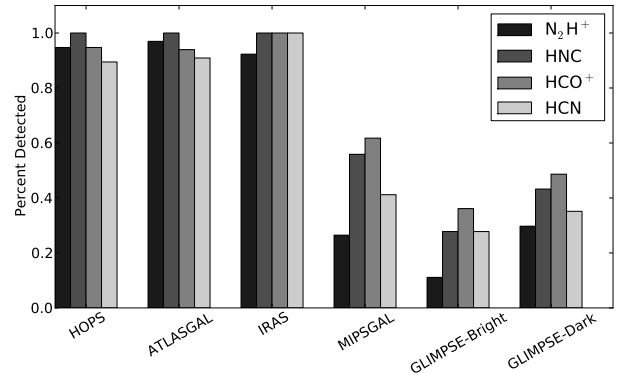


Figure 4. The percentage of robust detections of the four main pilot survey lines (N_2H^+ , HNC, HCO^+ , and HCN) as a function of input catalog. A robust detection is a source with maximum integrated intensity (M_0) $> 5\sigma_{M_0}$, excluding the poorly sampled edge 3 pixels ($27''$).

similar. We apply a two-sided Kolmogorov-Smirnov (K-S) test and find that we cannot reject the hypothesis that the HNC and HCO^+ line-widths are drawn from the same population when considering just the HCO^+ line-widths in sources without a H^{13}CO^+ detection (p-value = 9%) or all the HCO^+ line-widths (p-value = 32%).

The line-width distributions shown in Figure 8 are the line-widths at the positions of maximum integrated intensity for each molecular line transition. If we restrict our analysis to sources for which the positions of maximum integrated intensity for HCO^+ and HNC are within one $9''$ pixel (within $13''$ to include diagonally adjacent pixels) we can compare line-widths at roughly the same position. Figure 9 shows the results of this comparison for sources where $M_2/\sigma_{M_2} > 3$ in both lines. For the sources with an H^{13}CO^+ detection (i.e. where HCO^+ is likely to be optically thick) the HCO^+ line-width is typically larger than the HNC line-width ($\langle \Delta V_{\text{FWHM}}(\text{HCO}^+) - \Delta V_{\text{FWHM}}(\text{HNC}) \rangle = 1.15$). For the sources without an H^{13}CO^+ detection, the line-width ratios are correlated and centered around unity ($\langle \Delta V_{\text{FWHM}}(\text{HCO}^+) - \Delta V_{\text{FWHM}}(\text{HNC}) \rangle = 0.98$). This suggests that the sources with H^{13}CO^+ detections do have optically thick HCO^+ emission, and that this is what produces their larger line-widths. In the pilot survey, we have no rare isotopologue of HNC to study where HNC might be optically thick, but the main MALT90 survey will include HN^{13}C instead of H^{13}CN (HCN, because of its hyperfine structure, is less likely to be optically thick for similar line intensities).

5.2. Choice of Input Catalog

The first goal of the MALT90 pilot survey was to select an input catalog for the full MALT90 survey. Of the 6 catalogs tested, only HOPS, ATLASGAL and IRAS had sufficiently high ($> 90\%$) detection rates to be used as input catalogs for the main MALT90 survey. There are significant scientific and logistical benefits to using a single catalog when selecting sources. The main advantages are the ability to use a simple and uniform criteria for choosing sources, the ability to compare our observed line properties against properties of the input catalog, and the ability to describe the significance of non-detections.

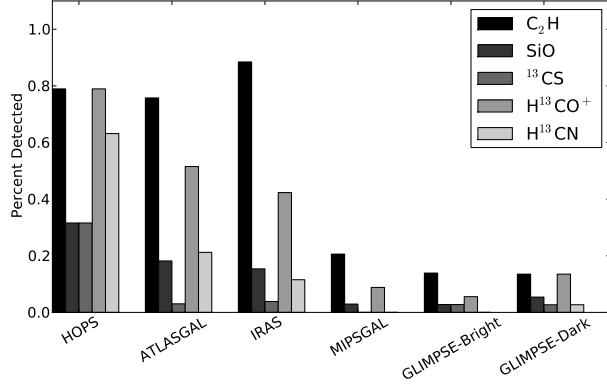


Figure 5. The percentage of robust detections of the frequently detected weaker pilot survey lines (C_2H , ^{13}CS , SiO , H^{13}CO^+ and H^{13}CN) as a function of input catalog. A robust detection is a source with maximum integrated intensity (M_0) $> 5\sigma_{M_0}$, excluding the poorly sampled edge 3 pixels ($27''$).

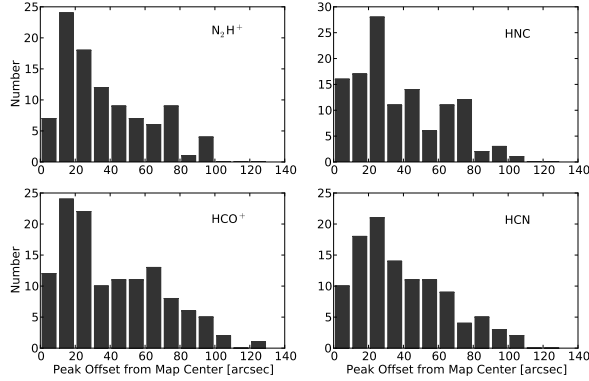


Figure 6. Radial offset of maximum integrated intensity for each of the four main MALT90 pilot lines (N_2H^+ , HNC , HCO^+ , and HCN) from the center of the map. Offsets are relative to the targeted center of the map, which is determined differently for the different input surveys. Pointing error is estimated to be less than $10''$.

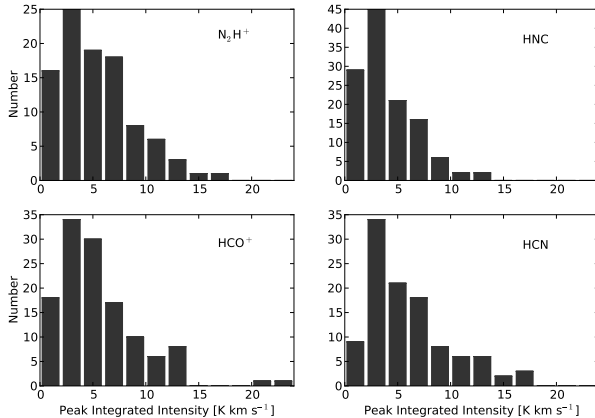


Figure 7. Maximum integrated intensity histograms of the four main species. The temperature scale is T_A^* . Detections are incomplete below 2 K km s^{-1} at the chosen 5σ level. The distributions for the four lines are broadly similar.

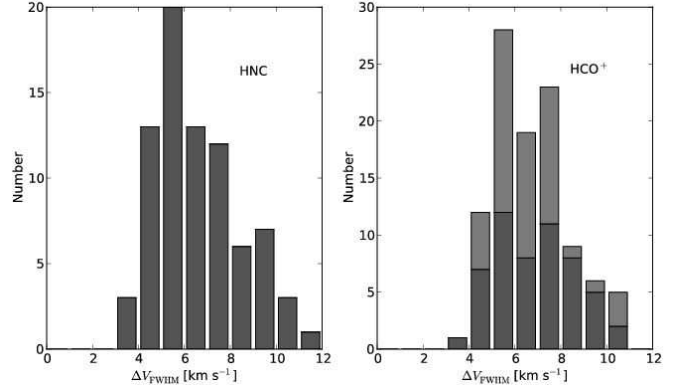


Figure 8. Effective ΔV_{FWHM} of the two strong single-component lines ([left] HNC and [right] HCO^+) where $M_2/\sigma_{M_2} > 3$. Light gray bars on the HCO^+ histogram show points with H^{13}CO^+ detections where the HCO^+ line is likely optically thick and self-absorbed. The distributions of line-widths are similar for the two lines.

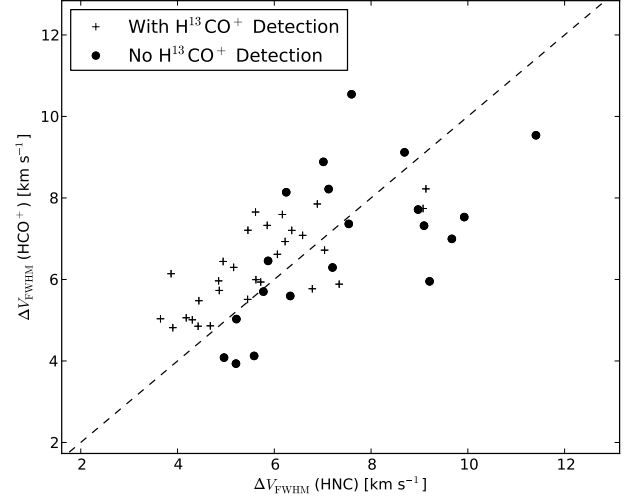


Figure 9. Comparison of the effective ΔV_{FWHM} of the two strong single-component lines ([left] HNC and [right] HCO^+) where the positions of maximum integrated intensity are within $13''$ and $M_2/\sigma_{M_2} > 3$. The dashed line is unity. Crosses indicate sources with H^{13}CO^+ detections where the HCO^+ line is likely optically thick and self-absorbed; in these sources the HCO^+ linewidth tends to have larger than the HNC linewidth. For the sources without H^{13}CO^+ detections, the linewidths are on average the same for both HCO^+ and HNC .

The ATLASGAL catalog provides the optimal source list for MALT90. There are three major factors in favor of using ATLASGAL: (1) catalog size, (2) a broad range of source positions and velocities, and (3) a range of evolutionary states.

ATLASGAL provides a much larger catalog than HOPS or the Beltrán et al. (2006) survey of IRAS sources. Schuller et al. (2009) report from the initial results of the survey about 6000 sources brighter than 0.25 Jy in 95 deg^2 in the Galactic range $-30^\circ \leq l \leq +11.5^\circ$ and $+15^\circ \leq b \leq +21^\circ$ with $|b| \leq 1^\circ$. In contrast the Beltrán et al. (2006) survey contains 235 sources and HOPS (Walsh et al. 2008) is expected to contain a few hundred bright NH_3 sources. Neither HOPS nor IRAS

contains a sufficient number of sources for the science goals of MALT90.

ATLASGAL sources appear to sample many Galactic structures. Figure 10 shows the Galactic longitude and velocity of sources with detections (using hand-determined velocities) plotted on the Dame et al. (2001) CO map. The Dame et al. (2001) CO map is presented as a longitude-velocity diagram integrated over $-2^\circ < b < 2^\circ$ and has units of K arcdeg. The positions of our sources in this plot all fall within the 0.3 K arcdeg CO contour and most cluster in the portions of stronger CO emission, as expected for dense, star-forming gas. The presence of ATLASGAL sources at many positions in the longitude-velocity diagram indicates that this catalog is detecting sources in a range of Galactic locations.

ATLASGAL sources cover a range of evolutionary states. The initial results of ATLASGAL found two-thirds of the sources do not have a mid- or far-infrared counterpart in the Midcourse Space Experiment (MSX) and IRAS catalogs. A closer inspection of IRAS/MSX dark sources in more sensitive *Spitzer* GLIMPSE/MIPSGAL images reveals many of them associated with weaker infrared sources but still a considerable fraction of the submillimeter emission appear dark in the *Spitzer* images (e.g., Fig. 13 and 14 of Schuller et al. 2009) and work on the first compact source release catalog demonstrates that ATLASGAL will provide enough sources in each evolutionary state as assessed by the *Spitzer* emission morphology scheme shown in Figure 1.

We thus choose ATLASGAL as the sole input catalog for the MALT90 survey because it meets all our requirements for a source list. ATLASGAL sources had high detection rates in this pilot survey, include a diversity of evolutionary states, and cover a broad range of Galactic positions. Choosing ATLASGAL as the sole input catalog also provides the benefits of having a single uniform catalog when selecting sources. We can choose our sources with a single uniform criteria and compare our MALT90 measurements against ATLASGAL catalog properties such as the flux and extent of 870 μm emission.

5.3. MALT90 Survey Strategy

The second goal MALT90 pilot survey was to test the observing set up and verify that it allows us to achieve our science goals. MALT90 is fundamentally a mapping survey; although some science goals (such as determining distances to clumps) could be achieved with a single pointing, the majority of our science goals rely on maps. Our configuration allows us to map sources in multiple lines at high spectral resolution. Maps of multiple lines allows us to study the chemical variation within a clump, which is most useful if clumps are typically spatially resolved and at least sometimes exhibit strong chemical variation. Mapping at high velocity resolution (0.11 km/s) allows us to study spatial variation in line profiles which may indicate changes in the strength of turbulence, large scale motions (rotation, shear, infall or outflow), or multiple velocity components. The pilot survey allowed us to verify that our on-the-fly maps had sufficient sensitivity and that we could make maps without significant artifacts.

5.3.1. Mapping Multiple Dense-gas Tracers to Reveal Chemistry

We see strong chemical variation in the MALT90 pilot sources which validates our decision to map multiple lines in these sources. All four of our main lines (N_2H^+ , HCN, HCO^+ and HNC) are ground state transitions of molecules with similar critical densities. As tracers of dense gas, the emission from these lines typically show similar morphologies in MALT90 pilot sources, but this is not always the case. Figure 11 shows two example sources where N_2H^+ varies significantly with respect to the other species. Figure 11 shows one source where the maximum N_2H^+ integrated intensity is a factor of 4-8 times weaker than the other three main lines. Conversely, the other source in Figure 11 has N_2H^+ emission which is twice as strong as that of HCN, HCN or HCO^+ . Large variation in the $\text{HCO}^+/\text{N}_2\text{H}^+$ integrated intensity ratio in high-mass star-forming regions has been noted before (e.g., Turner & Thaddeus 1977; Walsh & Burton 2006). Thus, the combination of mapping in several lines simultaneously gives us the most complete picture of the spatial distribution of the various molecules, which is crucial to studying variations in the chemistry with the MALT90 sources.

5.3.2. Mapping Strategy

Mapping artifacts are seen in many of our maps, typically manifesting as stripes in the direction of scans. Our sources were generally mapped with scans of constant Galactic longitude so that each strip in Galactic longitude uses the same reference spectrum. Noise or gain variations in this reference spectrum can therefore produce stripes in the map, and this phenomenon is particularly prevalent in sources observed in bad weather. We chose to map using scans of constant Galactic longitude for the pilot survey because most extended structures in the Galactic plane are parallel to the plane. Thus, noise stripes are easier to identify, since they typically run perpendicular to real features. We mapped two sources (G305.887+00.016 and G308.058–00.397) in both Galactic longitude and latitude to see if this would mitigate the striping. Figure 12 shows the two individual maps for G308.058–00.397 as well as the combination of both maps for a signal-free $^{13}\text{C}^{34}\text{S}$ cube. The striping visible in the scan direction in both individual maps is significantly reduced in the combined image. We therefore decided to map using scans of both constant Galactic longitude and latitude in the full MALT90 survey.

5.3.3. The Value of High-resolution Velocity Information

Figure 13 shows the central portion of the maps for the source G321.935–00.007 in HNC and HCO^+ . The HCO^+ line shows self-absorption at the systemic velocity (traced by the HNC which shows little or no non-gaussianity). In the lower-right portion of the map, this self-absorption shows an asymmetric profile with brighter blue-shifted emission. Such a profile is characteristic of infall of cold gas toward a hot central source (e.g., Mardones et al. 1997). This characteristic shape is not present in the upper-left of the map, where we see a red-shifted profile usually associated with expansion. It is possible that infall is happening only in part of this source or that other kinematic complexity is present; the

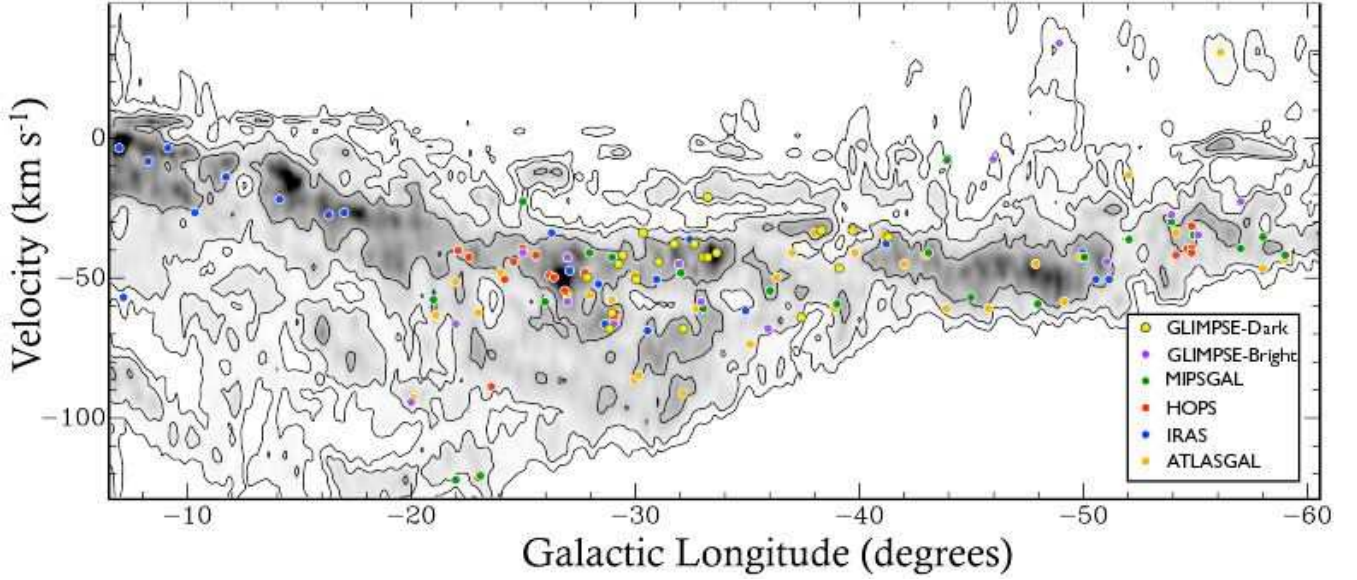


Figure 10. Distribution of MALT90 pilot sources in velocity and Galactic longitude, overlaid on the Galactic CO distribution from Dame et al. (2001) integrated over Galactic latitude. The CO contours are at 0.3, 1, 3, and 10 K arcdeg. Different input catalogs are labelled as follows: [yellow] = Dark GLIMPSE source, [purple] = Bright GLIMPSE source, [green] = MIPS GAL source, [red] = HOPS source, [blue] = IRAS source, [orange] = ALTAS GAL source. Sources with no detected line emission (and thus no velocity) are omitted. In addition, four IRAS sources with Galactic longitude between -70 and -100 degrees were omitted to display the remaining sources at a larger scale. These four omitted sources all also lie within the CO 0.3 K arcdeg emission contour.

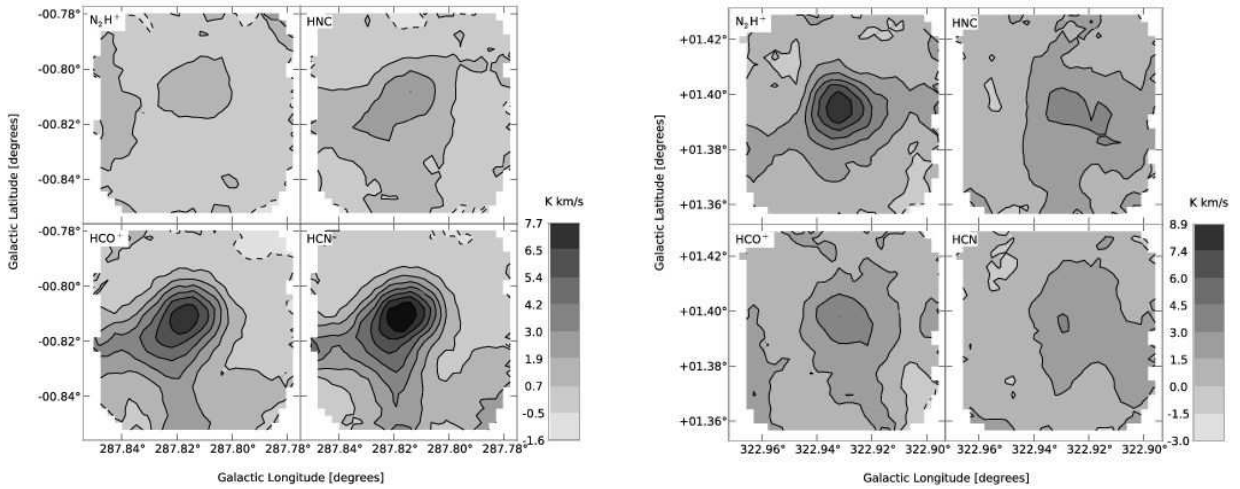


Figure 11. Two examples of strong chemical variation in N_2H^+ . Left: G287.814–00.816 shows strong (3–9 K km s^{−1}) HNC, HCO⁺, and HCN lines, but weak (1.65 ± 0.25 K km s^{−1}) N_2H^+ . Right: G322.932+01.393 shows a very strong N_2H^+ line (8.93 ± 0.33 K km s^{−1}), but comparatively weak HNC and HCO⁺ (3.5–4.5 K km s^{−1}) and a non-detection of HCN (< 1.66 K km s^{−1}).

large variance of this complex line shape over the source demonstrates the value of mapping at high velocity resolution.

5.3.4. Studying Different Stages of Evolution

The many lines observed in MALT90 provide information about the evolutionary state of the clumps observed. This information can be combined with *Spitzer* morphological classification and dust temperature determination from spectral-energy distribution fitting (e.g., Rathborne et al. 2010; Peretto et al. 2010) to constrain the evolutionary state of a clump. As a short example we present three sources in different *Spitzer* morphological states and show what information can be gained from the molecular lines in each case.

Figure 14 shows G330.873–00.361, a clump drawn

from the HOPS survey catalog and classified as an H II region from the *Spitzer* GLIMPSE/MIPSGAL images due to its strong extended 8 and 24 μm emission. The presence of CH_3CN ($J_K = 5_1 - 4_1$) emission identifies the hot core associated with a massive protostar since this molecule is seen only in warm ($T > 100$ K) and dense ($n > 10^5$ cm^{−3}) regions and is often detected in H II regions (e.g., Purcell et al. 2006). The location of the core is also the position of maximum integrated intensity for most of the other molecules (HCN, HNC, SiO, ¹³CS), but not N_2H^+ , which peaks in the south at the position of a 24 μm point source. Although this source is clearly identified as an H II region from the characteristic *Spitzer* appearance of a 24 μm inner bubble surrounded by a ring of 8 μm emission (e.g., Watson et al. 2008), the

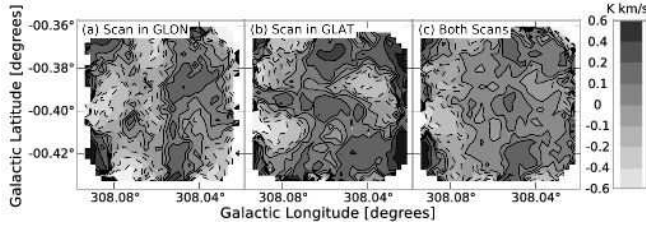


Figure 12. Zeroth moment (integrated intensity) maps of $^{13}\text{C}^{34}\text{S}$ in G308.058–00.397. $^{13}\text{C}^{34}\text{S}$ has very low abundance, so these maps show only noise. In panel (a) the map was made with scans of constant Galactic longitude, which is the default mode for the MALT90 pilot survey. In panel (b) the map was made with scans of constant Galactic latitude. In panel (c), the two individual maps were combined, reducing the striping artifacts visible in maps (a) and (b). This reduction of artificial structure motivates combining maps scanned in both directions in the full MALT90 Survey.

detection of a hot core molecule identifies the location of the central exciting source. The chemical difference ($\text{N}_2\text{H}^+/\text{HCO}^+$ ratio) between the southern source suggests either a different luminosity for the exciting source or a different evolutionary state.

Figure 15 shows G335.075–00.411, a clump drawn from the HOPS survey catalog and classified as protostellar from the *Spitzer* GLIMPSE/MIPSGAL images due to the presence of $24\ \mu\text{m}$ point sources within a dark extinction feature without extended 8 or $24\ \mu\text{m}$ emission. The spatial coincidence of the $24\ \mu\text{m}$ point sources and the $8\ \mu\text{m}$ extinction feature suggests that the $24\ \mu\text{m}$ point sources are associated with the clump, and the MALT90 pilot survey data confirms this association. The N_2H^+ integrated intensity contours trace the $8\ \mu\text{m}$ emission extinction feature. There is SiO emission at the same velocity at the position of the brightest $24\ \mu\text{m}$ point source. Since SiO emission is normally associated with outflow activity in protostars (e.g., López-Sepulcre et al. 2011), a detection of this line at the same velocity as the clump is strong evidence that the $24\ \mu\text{m}$ point source is associated with this clump.

Figure 16 shows G322.668–00.038, a clump drawn from the GLIMPSE-Dark catalog and classified as quiescent from the *Spitzer* GLIMPSE/MIPSGAL images due to the lack of 8 or $24\ \mu\text{m}$ emission inside the $8\ \mu\text{m}$ extinction feature. As a quiescent clump in the early stages of evolution, this object displays less complex chemistry than clumps in more evolved stages with only the four main lines (N_2H^+ , HNC, HCO^+ , and HCN) detected. The HNC integrated intensity emission shows two distinct peaks associated with two of the darkest $8\ \mu\text{m}$ extinction features. The velocity field of HNC shows that these two peaks are at very similar velocities ($-64\ \text{km s}^{-1}$ and $-65.6\ \text{km s}^{-1}$), strongly suggesting that both peaks are at the same distance and that the entire extinction feature is a single physical object. We use the Clemens (1985) rotation curve to calculate a kinematic distance for this clump; the near distance is 4.27 kpc and the far distance is 9.25 kpc. Because we see the clump as an extinction feature against the diffuse Galactic background, it is reasonable to assume that the near distance is correct. The MALT90 map therefore allows us (1) to identify which extinction features are likely a single physical object versus a chance projection and (2) to assign a distance which is useful for any further study of this object.

6. CONCLUSION

We have described the MALT90 pilot survey, carried out to demonstrate the feasibility of the MALT90 survey, identify the best input catalog for choosing MALT90 targets, and optimize the survey parameters. We choose the ATLASGAL (Schuller et al. 2009) catalog as our source list on the basis of its high detection rates for the main four survey lines ($> 90\%$ for N_2H^+ , HNC, HCO^+ , and HCN) and the large number of dense molecular clumps in different evolutionary stages in this catalog. The surveys which provided a prior selection for regions of high column density, either from optically-thin dust (ATLASGAL at $870\ \mu\text{m}$, the Beltrán et al. (2006) survey at 1.2-mm) or another dense gas tracer (NH_3 from HOPS) produced much higher detection rates than choosing sources identified based on *Spitzer* emission morphology without this prior.

We have briefly summarized the data obtained from the MALT90 pilot survey and highlighted some of the science possible with this survey including studying chemical variation, the kinematics of massive dense clumps and the galactic distribution of dense molecular clumps associated with high-mass star formation. We have made the full data-set publicly available through this publication and the MALT90 website, including reduced data-cubes and uniform moment maps which facilitate easy inspection of the data. This collection is already one of the largest sets of 90 GHz molecular line maps for dense molecular clumps. The full survey is underway and plans to map a total of 3,000 candidate dense molecular clumps, increasing this sample by an order of magnitude and providing a valuable database for studying many aspects of high-mass star formation.

7. ACKNOWLEDGEMENTS

The Mopra telescope is part of the Australia Telescope and is funded by the Commonwealth of Australia for operation as National Facility managed by CSIRO. The UNSW-MOPS Digital Filter Bank used for the observations with the Mopra telescope was provided with support from the Australian Research Council, together with the University of New South Wales, University of Sydney and Monash University. This research has made use of the NASA/ IPAC Infrared Science Archive (for access to GLIMPSE and MIPSGAL images), which is operated by the Jet Propulsion Laboratory, California Institute of Technology, under contract with the National Aeronautics and Space Administration. This research has made use of NASA’s Astrophysics Data System Bibliographic Services. JMJ gratefully acknowledges funding support from NSF Grant No. AST-0808001. The MALT90 project team gratefully acknowledges the use of dense core positions supplied by ATLASGAL. ATLASGAL is a collaboration between the Max Planck Gesellschaft (MPG: Max Planck Institute for Radioastronomy, Bonn and the Max Planck Institute for Astronomy, Heidelberg), the European Southern Observatory (ESO) and the University of Chile. Thanks to Anita Titmarsh and the duty astronomers and staff at the Paul Wild Observatory for their assistance during the observations.

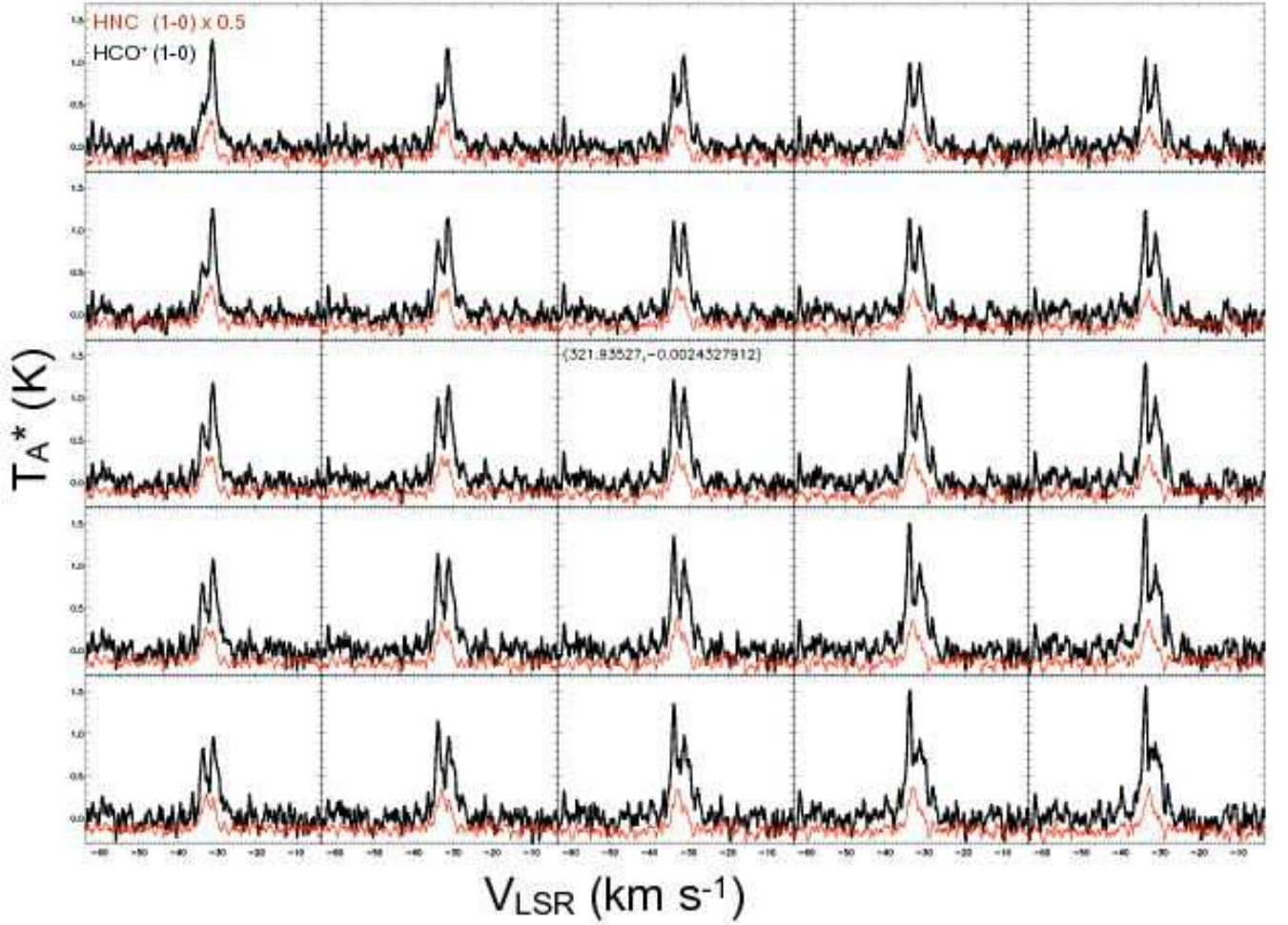


Figure 13. HCO^+ [thick/black] and HNC [thin/red] line profiles over the central portion of the G321.935–00.007 cube. The HNC spectra has been scaled by a factor of 0.5. The HCO^+ line shows a strong dip at the systemic velocity, but the relative strengths of the blue and red wings vary throughout this map. Adjacent spectra are separated by $9''$.

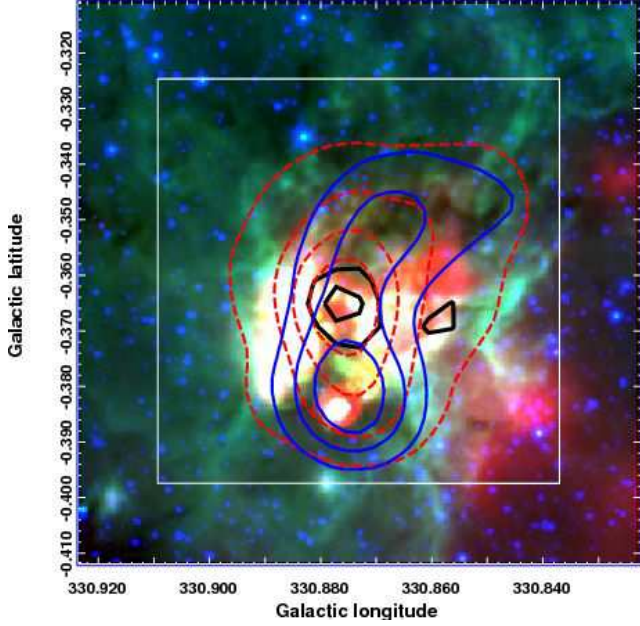


Figure 14. An example H II clump (G330.873–00.361) shown as a three color image with *Spitzer*/IRAC band 1 ($3.6 \mu\text{m}$) and band 4 ($8.0 \mu\text{m}$) from GLIMPSE in blue and green and *Spitzer*/MIPS band 1 ($24 \mu\text{m}$) from MIPS in red. The white box shows the extent of the MALT90 pilot survey map. Dashed (red) contours are HCO^+ integrated intensity (plotted at SNR of 15, 30, 45, 60; $\sigma \sim 0.25 \text{ K km s}^{-1}$). Thin (blue) contours are N_2H^+ integrated intensity (plotted at SNR of 10, 20, 30, 40; $\sigma \sim 0.26 \text{ K km s}^{-1}$). Thick (black) contours are CH_3CN integrated intensity (plotted at SNR of 2, 4; $\sigma \sim 0.28 \text{ K km s}^{-1}$). The presence of CH_3CN identifies the hot core associated with a massive protostar. This location is also the position of maximum integrated intensity for most of the other molecules (HCN , HNC , SiO , ^{13}CS), but N_2H^+ peaks in the south as the position of another $24 \mu\text{m}$ point source.

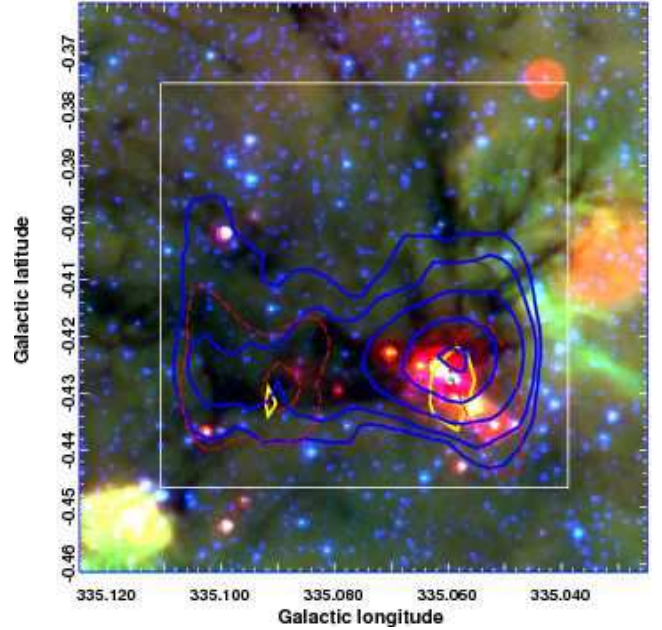


Figure 15. An example protostellar clump (G335.075–00.411) shown as a three color image with *Spitzer*/IRAC band 1 ($3.6 \mu\text{m}$) and band 4 ($8.0 \mu\text{m}$) from GLIMPSE in blue and green and *Spitzer*/MIPS band 1 ($24 \mu\text{m}$) from MIPS in red. The white box shows the extent of the MALT90 pilot survey map. Dashed (red) contours are HCO^+ integrated intensity (plotted at SNR of 5, 7; $\sigma \sim 0.30 \text{ K km s}^{-1}$). Thin (blue) contours are N_2H^+ integrated intensity (plotted at SNR of 7, 9, 13, 19, 25; $\sigma \sim 0.29 \text{ K km s}^{-1}$). Thick (yellow) contours are SiO integrated intensity (plotted at SNR of 4; $\sigma \sim 0.20 \text{ K km s}^{-1}$ in the small velocity window). This clump was drawn from the HOPS catalog and classified as protostellar due to the presence of several $24 \mu\text{m}$ point sources. The strongest $24 \mu\text{m}$ point sources are associated with SiO emission at the same velocity as the clump, indicating the presence of protostellar outflows in the clump.

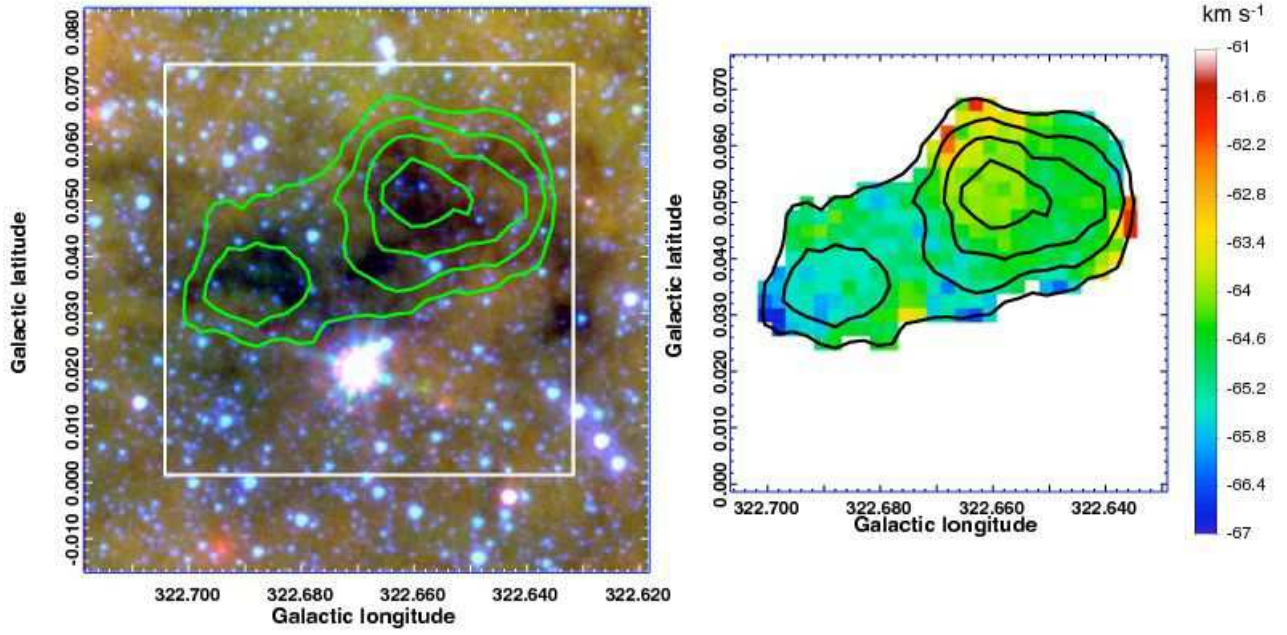


Figure 16. An example quiescent clump (G322.668–00.038) shown (left) as a three color image with *Spitzer*/IRAC band 1 ($3.6 \mu\text{m}$) and band 4 ($8.0 \mu\text{m}$) from GLIMPSE in blue and green and *Spitzer*/MIPS band 1 ($24 \mu\text{m}$) from MIPS GAL in red. The white box shows the extent of the MALT90 pilot survey map. The extinction seen at $8.0 \mu\text{m}$ is well traced by the HNC integrated intensity contours (plotted as SNR of 4, 6, 8, 10; $\sigma \sim 0.25 \text{ K km s}^{-1}$) which show two distinct peaks. The right panel shows the centroid velocity M_1 in color with the HNC integrated intensity contours. The two peaks are at very similar velocities (-64 km s^{-1} and -65.5 km s^{-1} , suggesting that the extinction feature is all at the same distance).

REFERENCES

- Beltrán, M. T., Brand, J., Cesaroni, R., et al. 2006, *A&A*, 447, 221
- Benjamin, R. A., Churchwell, E., Babler, B. L., et al. 2003, *PASP*, 115, 953
- Bergin, E. A., Ciardi, D. R., Lada, C. J., Alves, J., & Lada, E. A. 2001, *ApJ*, 557, 209
- Bergin, E. A. & Tafalla, M. 2007, *ARA&A*, 45, 339
- Brown, P. D., Charnley, S. B., & Millar, T. J. 1988, *MNRAS*, 231, 409
- Carey, S. J., Noriega-Crespo, A., Mizuno, D. R., et al. 2009, *PASP*, 121, 76
- Clemens, D. P. 1985, *ApJ*, 295, 422
- Dame, T. M., Hartmann, D., & Thaddeus, P. 2001, *ApJ*, 547, 792
- Fazio, G. G., Hora, J. L., Allen, L. E., et al. 2004, *ApJS*, 154, 10
- Fuller, G. A., Williams, S. J., & Sridharan, T. K. 2005, *A&A*, 442, 949
- Gerin, M., Kaźmierczak, M., Jastrzebska, M., et al. 2011, *A&A*, 525, A116+
- Gibson, D., Plume, R., Bergin, E., Ragan, S., & Evans, N. 2009, *ApJ*, 705, 123
- Hirota, T., Yamamoto, S., Mikami, H., & Ohishi, M. 1998, *ApJ*, 503, 717
- Jackson, J. M., Finn, S. C., Rathborne, J. M., Chambers, E. T., & Simon, R. 2008, *ApJ*, 680, 349
- Ladd, N., Purcell, C., Wong, T., & Robertson, S. 2005, *PASA*, 22, 62
- Lo, N., Cunningham, M. R., Jones, P. A., et al. 2009, *MNRAS*, 395, 1021
- López-Sepulcre, A., Walmsley, C. M., Cesaroni, R., et al. 2011, *A&A*, 526, L2+
- Mardones, D., Myers, P. C., Tafalla, M., et al. 1997, *ApJ*, 489, 719
- Peretto, N. & Fuller, G. A. 2009, *A&A*, 505, 405
- Peretto, N., Fuller, G. A., Plume, R., et al. 2010, *A&A*, 518, L98+
- Pirogov, L., Zinchenko, I., Caselli, P., Johansson, L. E. B., & Myers, P. C. 2003, *A&A*, 405, 639
- Purcell, C. R., Balasubramanyam, R., Burton, M. G., et al. 2006, *MNRAS*, 367, 553
- Rathborne, J. M., Jackson, J. M., Chambers, E. T., et al. 2010, *ApJ*, 715, 310
- Rawlings, J. M. C., Redman, M. P., Keto, E., & Williams, D. A. 2004, *MNRAS*, 351, 1054
- Rieke, G. H., Young, E. T., Engelbracht, C. W., et al. 2004, *ApJS*, 154, 25
- Schilke, P., Walmsley, C. M., Pineau des Forets, G., & Flower, D. R. 1997, *A&A*, 321, 293
- Schuller, F., Menten, K. M., Contreras, Y., et al. 2009, *A&A*, 504, 415
- Shirley, Y. L., Evans, II, N. J., Young, K. E., Knez, C., & Jaffe, D. T. 2003, *ApJS*, 149, 375
- Shukla, H., Yun, M. S., & Scoville, N. Z. 2004, *ApJ*, 616, 231
- Simon, R., Jackson, J. M., Rathborne, J. M., & Chambers, E. T. 2006, *ApJ*, 639, 227
- Turner, B. E. & Thaddeus, P. 1977, *ApJ*, 211, 755
- Walsh, A. J. & Burton, M. G. 2006, *MNRAS*, 365, 321
- Walsh, A. J., Lo, N., Burton, M. G., et al. 2008, *PASA*, 25, 105
- Watson, C., Povich, M. S., Churchwell, E. B., et al. 2008, *ApJ*, 681, 1341
- Williams, J. P., Blitz, L., & McKee, C. F. 2000, *Protostars and Planets IV*, 97
- Wu, J., Evans, N. J., Shirley, Y. L., & Knez, C. 2010, *ApJS*, 188, 313

Table 3
MALT90 Pilot Sources

Name	Glon [degrees]	Glat [degrees]	RA J2000 [HH:MM:SS]	Dec J2000 [DD:MM:SS]	Catalog	Velocity LSR [km s ⁻¹]	T _{rms} [K]
G263.620-00.530	263.620	-0.530	08:45:36.003	-43:51:01.99	IRAS	+4.72	0.282
G264.322-00.184	264.322	-0.184	08:49:32.995	-44:10:46.19	IRAS	+9.07	0.364
G285.259-00.049	285.259	-0.049	10:31:28.383	-58:02:07.23	IRAS	+2.14	0.199
G287.814-00.816	287.814	-0.816	10:45:53.955	-59:57:01.87	IRAS	-14.96	0.195
G300.958+00.902	300.958	+0.902	12:34:39.728	-61:54:19.57	MIPSGAL	-41.67	0.209
G300.960-00.702	300.960	-0.702	12:33:44.636	-63:30:21.53	GLIMPSE-Bright	...	0.208
G300.968+01.145	300.968	+1.145	12:34:52.771	-61:39:48.93	ATLASGAL	-42.96	0.197
G301.991-00.704	301.991	-0.704	12:42:59.051	-63:33:37.09	GLIMPSE-Bright	...	0.177
G302.018-00.113	302.018	-0.113	12:43:23.547	-62:58:13.69	MIPSGAL	-35.17	0.181
G302.021+00.251	302.021	+0.251	12:43:31.042	-62:36:24.26	ATLASGAL	-46.45	0.190
G302.989+00.352	302.989	+0.352	12:51:55.963	-62:31:10.89	MIPSGAL	-39.89	0.206
G303.000-00.446	303.000	-0.446	12:52:02.662	-63:19:03.60	GLIMPSE-Bright	-22.76	0.204
G303.932-00.688	303.932	-0.688	13:00:25.067	-63:32:32.31	ATLASGAL	+30.60	0.274
G303.980-00.033	303.980	-0.033	13:00:38.302	-62:53:09.68	MIPSGAL	...	0.322
G303.992+00.209	303.992	+0.209	13:00:40.051	-62:38:37.49	GLIMPSE-Bright	...	0.187
G304.887+00.635	304.887	+0.635	13:08:12.094	-62:10:23.14	ATLASGAL	-36.52	0.244
G305.034+00.021	305.034	+0.021	13:09:50.002	-62:46:32.31	GLIMPSE-Bright	-34.75	0.224
G305.044+00.573	305.044	+0.573	13:09:34.852	-62:13:27.56	MIPSGAL	-34.89	0.210
G305.190+00.210	305.190	+0.210	13:11:04.056	-62:34:32.35	HOPS	-40.84	0.210
G305.232+00.277	305.232	+0.277	13:11:23.174	-62:30:20.25	HOPS	-39.51	0.261
G305.264-00.018	305.264	-0.018	13:11:51.907	-62:47:49.98	HOPS	-32.51	0.157
G305.357+00.193	305.357	+0.193	13:12:31.510	-62:34:45.89	HOPS	-38.75	0.277
G305.807-00.107	305.807	-0.107	13:16:40.202	-62:50:16.11	HOPS	-42.21	0.321
G305.887+00.016	305.887	+0.016	13:17:15.579	-62:42:26.99	ATLASGAL	-33.97	0.311
G306.033+00.034	306.033	+0.034	13:18:30.587	-62:40:28.67	MIPSGAL	-29.83	0.214
G306.053-00.040	306.053	-0.040	13:18:45.079	-62:44:46.00	GLIMPSE-Bright	-28.07	0.245
G306.989-00.512	306.989	-0.512	13:27:25.380	-63:05:59.77	GLIMPSE-Bright	...	0.204
G307.017+00.706	307.017	+0.706	13:26:13.164	-61:53:22.42	MIPSGAL	...	0.188
G308.006-00.388	308.006	-0.388	13:36:05.525	-62:49:08.39	MIPSGAL	-36.64	0.209
G308.037+00.250	308.037	+0.250	13:35:24.687	-62:11:06.34	GLIMPSE-Bright	...	0.248
G308.058-00.397	308.058	-0.397	13:36:33.251	-62:49:07.88	ATLASGAL	-13.37	0.211
G308.914+00.126	308.914	+0.126	13:42:59.511	-62:08:43.72	IRAS	-50.56	0.235
G309.001-00.030	309.001	-0.030	13:43:59.486	-62:16:51.16	MIPSGAL	...	0.204
G309.014+00.208	309.014	+0.208	13:43:41.355	-62:02:42.53	GLIMPSE-Bright	-44.49	0.201
G309.378-00.142	309.378	-0.142	13:47:21.891	-62:18:42.28	IRAS	-50.89	0.200
G310.004+00.503	310.004	+0.503	13:51:19.958	-61:32:36.98	MIPSGAL	-41.67	0.208
G310.008-00.022	310.008	-0.022	13:52:23.778	-62:03:12.10	GLIMPSE-Bright	...	0.208
G310.013+00.389	310.013	+0.389	13:51:37.636	-61:39:08.86	IRAS	-41.39	0.218
G310.013+00.387	310.013	+0.387	13:51:37.870	-61:39:15.87	ATLASGAL	-41.56	0.255
G310.880+00.004	310.880	+0.004	13:59:31.500	-61:48:45.12	ATLASGAL	-58.10	0.267
G310.988-00.957	310.988	-0.957	14:02:37.129	-62:42:36.35	MIPSGAL	...	0.210
G311.005-00.362	311.005	-0.362	14:01:22.423	-62:07:57.21	GLIMPSE-Bright	+34.53	0.201
G312.006+00.178	312.006	+0.178	14:08:12.797	-61:20:01.66	GLIMPSE-Bright	...	0.197
G312.038+00.077	312.038	+0.077	14:08:42.975	-61:25:15.43	MIPSGAL	-59.48	0.197
G312.071+00.080	312.071	+0.080	14:08:58.348	-61:24:30.07	ATLASGAL	-44.41	0.251
G312.992+00.172	312.992	+0.172	14:16:01.019	-61:02:12.86	GLIMPSE-Bright	...	0.215
G313.015-00.384	313.015	-0.384	14:17:41.936	-61:33:19.61	MIPSGAL	...	0.234
G313.976+00.139	313.976	+0.139	14:23:43.849	-60:44:18.12	MIPSGAL	...	0.231
G313.994-00.084	313.994	-0.084	14:24:30.618	-60:56:27.39	GLIMPSE-Bright	-7.37	0.237
G314.219+00.271	314.219	+0.271	14:25:12.485	-60:31:45.80	ATLASGAL	-60.76	0.236
G314.994+00.096	314.994	+0.096	14:31:34.901	-60:24:32.80	MIPSGAL	-56.76	0.212
G314.995-00.073	314.995	-0.073	14:32:06.439	-60:33:54.81	GLIMPSE-Bright	...	0.208
G315.981-00.187	315.981	-0.187	14:39:49.260	-60:17:00.90	MIPSGAL	-7.99	0.200
G315.985-00.605	315.985	-0.605	14:41:14.055	-60:39:49.00	GLIMPSE-Bright	...	0.206
G316.139-00.504	316.139	-0.504	14:42:02.319	-60:30:29.43	ATLASGAL	-60.99	0.224
G316.944+00.303	316.944	+0.303	14:45:11.036	-59:26:18.13	MIPSGAL	-40.89	0.222
G316.958+00.302	316.958	+0.302	14:45:17.220	-59:26:00.02	ATLASGAL	-41.22	0.229
G316.963+00.022	316.963	+0.022	14:46:15.842	-59:41:04.41	GLIMPSE-Bright	...	0.213
G317.106-00.015	317.106	-0.015	14:47:24.772	-59:39:23.63	GLIMPSE-Dark	...	0.212
G317.242+00.017	317.242	+0.017	14:48:16.369	-59:34:07.85	GLIMPSE-Dark	...	0.200
G317.977-00.011	317.977	-0.011	14:53:33.035	-59:16:05.40	MIPSGAL	...	0.203
G318.049+00.086	318.049	+0.086	14:53:42.569	-59:08:56.72	ATLASGAL	-50.50	0.261
G318.062-00.083	318.062	-0.083	14:54:23.968	-59:17:37.64	GLIMPSE-Bright	...	0.209
G318.145-00.764	318.145	-0.764	14:57:27.375	-59:51:37.02	GLIMPSE-Dark	...	0.202
G318.776-00.151	318.776	-0.151	14:59:34.903	-59:01:23.04	IRAS	-37.75	0.202
G318.786-00.397	318.786	-0.397	15:00:33.529	-59:14:05.92	GLIMPSE-Dark	...	0.231
G318.916-00.284	318.916	-0.284	15:01:01.858	-59:04:25.38	GLIMPSE-Dark	-35.29	0.239
G318.948-00.197	318.948	-0.197	15:00:55.636	-58:58:55.14	ATLASGAL	-34.86	0.262
G318.982+00.323	318.982	+0.323	14:59:15.526	-58:30:28.57	GLIMPSE-Bright	...	0.201
G319.033-00.422	319.033	-0.422	15:02:20.763	-59:08:19.71	MIPSGAL	...	0.199
G319.990+00.368	319.990	+0.368	15:05:48.456	-57:58:58.24	MIPSGAL	...	0.209
G320.019-00.158	320.019	-0.158	15:07:58.746	-58:25:30.81	GLIMPSE-Bright	...	0.216
G320.168+00.824	320.168	+0.824	15:05:17.352	-57:29:53.70	ATLASGAL	-40.70	0.205
G320.270+00.293	320.270	+0.293	15:07:55.231	-57:54:32.91	GLIMPSE-Dark	-32.81	0.215
G320.874-00.351	320.874	-0.351	15:14:19.570	-58:09:20.14	GLIMPSE-Dark	-46.14	0.203

Table 3 — *Continued*

Name	Glon [degrees]	Glat [degrees]	RA J2000 [HH:MM:SS]	Dec J2000 [DD:MM:SS]	Catalog	Velocity LSR [km s ⁻¹]	T _{rms} [K]
G321.013-00.522	321.013	-0.522	15:15:54.204	-58:13:43.90	MIPSGAL	-60.34	0.201
G321.024-00.699	321.024	-0.699	15:16:40.988	-58:22:25.07	GLIMPSE-Bright	...	0.201
G321.030-00.483	321.030	-0.483	15:15:51.478	-58:11:12.27	ATLASGAL	-60.23	0.187
G321.709+00.062	321.709	+0.062	15:18:01.566	-57:21:55.59	GLIMPSE-Dark	-32.23	0.199
G321.935-00.007	321.935	-0.007	15:19:42.921	-57:18:11.29	ATLASGAL	-33.24	0.225
G321.988+00.312	321.988	+0.312	15:18:47.211	-57:00:19.00	MIPSGAL	...	0.213
G322.032-00.063	322.032	-0.063	15:20:32.631	-57:17:53.48	GLIMPSE-Bright	...	0.205
G322.668+00.038	322.668	+0.038	15:24:03.949	-56:52:01.88	GLIMPSE-Dark	-64.46	0.210
G322.932+01.393	322.932	+1.393	15:20:21.190	-55:35:12.23	ATLASGAL	-40.79	0.251
G323.740-00.263	323.740	-0.263	15:31:45.498	-56:30:51.42	ATLASGAL	-49.61	0.241
G323.921+00.400	323.921	+0.400	15:30:06.447	-55:51:59.48	MIPSGAL	-54.76	0.213
G324.017-00.399	324.017	-0.399	15:33:57.977	-56:27:56.85	GLIMPSE-Bright	-68.47	0.219
G324.922-00.570	324.922	-0.570	15:39:57.733	-56:04:17.73	ATLASGAL	-73.82	0.241
G325.004-00.408	325.004	-0.408	15:39:44.488	-55:53:33.60	MIPSGAL	...	0.198
G325.030+00.051	325.030	+0.051	15:37:57.315	-55:30:28.49	GLIMPSE-Bright	...	0.199
G325.127+00.029	325.127	+0.029	15:38:35.943	-55:28:05.53	IRAS	-61.99	0.207
G326.369-00.563	326.369	-0.563	15:48:04.005	-55:11:07.11	GLIMPSE-Dark	...	0.286
G326.410+00.596	326.410	+0.596	15:43:22.064	-54:14:41.27	GLIMPSE-Dark	-41.25	0.199
G326.668-00.732	326.668	-0.732	15:50:26.471	-55:07:51.94	GLIMPSE-Dark	...	0.200
G326.794+00.386	326.794	+0.386	15:46:19.471	-54:10:35.16	GLIMPSE-Dark	-21.32/-42.40	0.201
G326.939+00.562	326.939	+0.562	15:46:21.939	-53:56:54.53	GLIMPSE-Dark	-42.41	0.224
G326.987-00.030	326.987	-0.030	15:49:07.644	-54:23:01.21	GLIMPSE-Bright	-59.05	0.237
G326.989-00.032	326.989	-0.032	15:49:08.802	-54:23:02.36	ATLASGAL	-59.50	0.201
G326.989-00.032	326.989	-0.032	15:49:08.802	-54:23:02.36	ATLASGAL	-59.46	0.201
G327.005-00.754	327.005	-0.754	15:52:21.942	-54:56:10.12	GLIMPSE-Dark	...	0.231
G327.054+00.037	327.054	+0.037	15:49:12.033	-54:17:22.27	MIPSGAL	-61.31	0.301
G327.135-00.262	327.135	-0.262	15:50:55.150	-54:28:19.68	IRAS	-61.38	0.321
G327.253-00.093	327.253	-0.093	15:50:49.284	-54:15:59.43	GLIMPSE-Dark	...	0.191
G327.397-00.743	327.397	-0.743	15:54:25.168	-54:40:43.88	GLIMPSE-Dark	-37.63	0.188
G327.574-00.851	327.574	-0.851	15:55:50.289	-54:38:55.40	IRAS	-36.77	0.249
G327.858-00.583	327.858	-0.583	15:56:09.194	-54:15:39.40	GLIMPSE-Dark	-67.12/-47.99	0.203
G327.895+00.150	327.895	+0.150	15:53:09.985	-53:40:22.65	ATLASGAL	-91.27	0.203
G327.937+00.511	327.937	+0.511	15:51:50.984	-53:22:00.17	GLIMPSE-Dark	...	0.203
G327.981-00.005	327.981	-0.005	15:54:16.847	-53:44:16.68	MIPSGAL	-47.81	0.223
G327.994+00.376	327.994	+0.376	15:52:43.098	-53:26:07.33	GLIMPSE-Bright	-44.73	0.214
G328.255-00.410	328.255	-0.410	15:57:27.854	-53:52:22.65	GLIMPSE-Dark	-38.37	0.201
G328.694+00.255	328.694	+0.255	15:56:50.247	-53:04:53.76	GLIMPSE-Dark	...	0.255
G328.971+00.019	328.971	+0.019	15:59:15.645	-53:04:56.03	GLIMPSE-Dark	...	0.241
G329.034-00.674	329.034	-0.674	16:02:37.129	-53:33:52.96	GLIMPSE-Dark	...	0.204
G329.036-00.198	329.036	-0.198	16:00:31.983	-53:12:15.68	GLIMPSE-Dark	-44.67	0.223
G329.183-00.313	329.183	-0.313	16:01:46.662	-53:11:41.51	IRAS	-50.56	0.256
G329.370-00.337	329.370	-0.337	16:02:49.297	-53:05:23.28	GLIMPSE-Dark	...	0.245
G329.457+00.506	329.457	+0.506	15:59:36.246	-52:23:46.27	IRAS	-68.63	0.246
G329.643-00.456	329.643	-0.456	16:04:42.414	-52:59:53.43	GLIMPSE-Dark	-34.31	0.187
G329.816+00.140	329.816	+0.140	16:02:57.339	-52:26:13.52	ATLASGAL	-85.43	0.236
G330.030+01.045	330.030	+1.045	16:00:08.557	-51:36:50.16	ATLASGAL	-48.45/-86.11	0.211
G330.042+01.059	330.042	+1.059	16:00:08.537	-51:35:43.78	GLIMPSE-Dark	-48.76	0.229
G330.042-00.058	330.042	-0.058	16:04:55.623	-52:26:08.16	GLIMPSE-Bright	...	0.350
G330.346-00.026	330.346	-0.026	16:06:16.182	-52:12:32.39	GLIMPSE-Dark	...	0.232
G330.620-00.221	330.620	-0.221	16:08:26.928	-52:10:10.23	GLIMPSE-Dark	...	0.234
G330.778+00.256	330.778	+0.256	16:07:07.552	-51:42:36.89	GLIMPSE-Dark	-44.32	0.239
G330.873-00.361	330.873	-0.361	16:10:16.810	-52:06:05.15	HOPS	-62.76	0.212
G330.948-00.504	330.948	-0.504	16:11:16.327	-52:09:18.91	GLIMPSE-Dark	-62.55	0.201
G330.986+00.330	330.986	+0.330	16:07:47.890	-51:30:56.55	ATLASGAL	-56.96	0.226
G330.997-00.507	330.997	-0.507	16:11:31.146	-52:07:26.57	GLIMPSE-Bright	-66.06	0.220
G331.032-00.419	331.032	-0.419	16:11:17.718	-52:02:08.90	HOPS	-64.80	0.212
G331.035+00.276	331.035	+0.276	16:08:15.886	-51:31:21.55	MIPSGAL	-42.52	0.196
G331.221+00.012	331.221	+0.012	16:10:17.698	-51:35:28.70	GLIMPSE-Dark	...	0.210
G331.230-00.420	331.230	-0.420	16:12:14.348	-51:54:04.98	GLIMPSE-Dark	-42.44/-67.41	0.214
G331.333-00.338	331.333	-0.338	16:12:21.751	-51:46:16.02	IRAS	-66.05	0.201
G331.620+00.522	331.620	+0.522	16:09:57.395	-50:56:45.39	IRAS	-52.32	0.236
G331.748+00.412	331.748	+0.412	16:11:01.634	-50:56:22.89	GLIMPSE-Dark	...	0.232
G331.914-00.320	331.914	-0.320	16:14:59.899	-51:21:31.31	GLIMPSE-Dark	...	0.228
G332.003-00.129	332.003	-0.129	16:14:34.055	-51:09:32.56	GLIMPSE-Bright	...	0.243
G332.070+00.503	332.070	+0.503	16:12:07.464	-50:39:12.63	MIPSGAL	-40.52	0.216
G332.093-00.421	332.093	-0.421	16:16:16.378	-51:18:27.73	ATLASGAL	-56.31	0.233
G332.190-00.047	332.190	-0.047	16:15:04.125	-50:58:14.33	GLIMPSE-Dark	-48.54	0.229
G332.233-00.036	332.233	-0.036	16:15:13.072	-50:55:58.75	HOPS	-48.28	0.224
G332.258-00.196	332.258	-0.196	16:16:02.166	-51:01:52.21	GLIMPSE-Dark	...	0.231
G332.963+00.773	332.963	+0.773	16:15:01.332	-49:50:37.59	IRAS	-46.98	0.226
G333.000-00.436	333.000	-0.436	16:20:27.787	-50:41:04.74	ATLASGAL	-56.01	0.236
G333.030-00.015	333.030	-0.015	16:18:44.332	-50:21:49.15	GLIMPSE-Bright	-42.24/-58.42	0.227
G333.067-00.444	333.067	-0.444	16:20:47.931	-50:38:35.34	HOPS	-54.24	0.248
G333.508-00.253	333.508	-0.253	16:21:54.805	-50:11:47.65	HOPS	-50.07	0.264
G333.726+00.366	333.726	+0.366	16:20:09.768	-49:36:14.15	IRAS	-33.91	0.239

Table 3 — *Continued*

Name	Gl _{on} [degrees]	Gl _{at} [degrees]	RA J2000 [HH:MM:SS]	Dec J2000 [DD:MM:SS]	Catalog	Velocity LSR [km s ⁻¹]	T _{rms} [K]
G333.767−00.269	333.767	−0.269	16:23:07.437	−50:01:27.57	HOPS	−49.52	0.242
G334.050+00.352	334.050	+0.352	16:21:38.340	−49:23:07.82	MIPSGAL	−57.71	0.222
G334.458−00.244	334.458	−0.244	16:26:00.739	−49:30:49.81	HOPS	−41.64	0.202
G334.975−00.048	334.975	−0.048	16:27:21.243	−49:00:22.01	MIPSGAL	−22.70	0.206
G335.060−00.427	335.060	−0.427	16:29:23.135	−49:12:24.86	GLIMPSE-Bright	−39.95	0.223
G335.075−00.411	335.075	−0.411	16:29:22.676	−49:11:06.03	HOPS	−39.67	0.220
G335.434−00.236	335.434	−0.236	16:30:06.658	−48:48:14.98	HOPS	−44.62	0.233
G335.800+00.181	335.800	+0.181	16:29:48.239	−48:15:05.97	HOPS	−50.17	0.246
G335.988−00.561	335.988	−0.561	16:33:50.644	−48:37:17.92	GLIMPSE-Bright	...	0.220
G336.022−00.816	336.022	−0.816	16:35:07.239	−48:46:09.52	ATLASGAL	−47.80	0.233
G336.426−00.253	336.426	−0.253	16:34:16.191	−48:05:27.22	HOPS	−88.41	0.400
G336.991+00.184	336.991	+0.184	16:34:38.026	−47:22:45.27	GLIMPSE-Bright	...	0.238
G336.994−00.019	336.994	−0.019	16:35:31.845	−47:30:51.20	HOPS/MIPSGAL	−120.88	0.246
G337.004+00.325	337.004	+0.325	16:34:04.426	−47:16:26.93	ATLASGAL	−62.64	0.228
G337.436−00.394	337.436	−0.394	16:38:55.876	−47:26:16.48	HOPS	−41.87	0.208
G337.912−00.469	337.912	−0.469	16:41:07.546	−47:07:54.60	HOPS	−40.33	0.237
G337.994−00.136	337.994	−0.136	16:39:58.940	−46:50:58.96	GLIMPSE-Bright	−66.28	0.231
G337.994+00.078	337.994	+0.078	16:39:02.949	−46:42:26.41	MIPSGAL	−122.31	0.229
G337.995+00.133	337.995	+0.133	16:38:48.840	−46:40:11.72	ATLASGAL	−50.84	0.251
G338.927+00.635	338.927	+0.635	16:40:13.801	−45:38:24.50	ATLASGAL	−63.43	0.229
G339.007+00.436	339.007	+0.436	16:41:23.217	−45:42:43.10	MIPSGAL	−57.12	0.228
G339.028+00.124	339.028	+0.124	16:42:48.762	−45:54:06.63	GLIMPSE-Bright	...	0.232
G339.968−00.529	339.968	−0.529	16:49:09.637	−45:36:42.93	ATLASGAL/GLIMPSE-Bright	−94.05	0.250
G340.114+00.474	340.114	+0.474	16:45:21.186	−44:51:06.02	MIPSGAL	...	0.405
G342.975+02.673	342.975	+2.673	16:46:22.662	−41:14:56.65	IRAS	−26.40	0.211
G343.722−00.221	343.722	−0.221	17:00:57.901	−42:29:54.63	IRAS	−27.92	0.214
G345.889−01.104	345.889	−1.104	17:11:46.145	−41:18:03.71	IRAS	−21.88	0.199
G348.236−00.976	348.236	−0.976	17:18:23.882	−39:19:10.15	IRAS	−13.30	0.193
G349.642−01.093	349.642	−1.093	17:23:00.379	−38:13:54.13	IRAS	−26.82	0.188
G350.884+00.734	350.884	+0.734	17:19:01.355	−36:10:11.46	IRAS	−3.76	0.178
G351.695−01.148	351.695	−1.148	17:29:00.935	−36:33:38.76	IRAS	−8.97	0.190
G352.859−00.204	352.859	−0.204	17:28:19.077	−35:04:07.86	IRAS	−56.37	0.186
G353.057+00.542	353.057	+0.542	17:25:50.306	−34:29:19.56	IRAS	−3.41	0.215

Note. — Central source velocities are determined by hand-examination of the four main lines for each source. Where two velocity components are seen, the stronger is listed first. T_{rms} gives the noise per channel in the spectrum as measured at the central position in the map.

Table 4
Properties of Main Lines at Position of Maximum Integrated Intensity

Name	Maximum Integrated Intensity [K km s ⁻¹]				Offset from Map Center ^a [9'' pixels]				FWHM [km s ⁻¹]	
	N ₂ H ⁺	HNC	HCO ⁺	HCN	N ₂ H ⁺	HNC	HCO ⁺	HCN	HNC	HCO ⁺
G263.620-00.530	2.47±0.42	2.95±0.38	5.09±0.39	5.18±0.38	(9, -2)	(-4, -5)	(-5, -5)	(-4, -4)	6.33±1.59	5.59±1.09
G264.322-00.184	3.58±0.57	3.15±0.49	3.82±0.56	4.16±0.46	(-9, -2)	(-7, -3)	(-9, -4)	(-4, -3)	6.18±1.90	3.95±4.01
G285.259-00.049	4.03±0.25	4.34±0.26	13.07±0.27	12.42±0.28	(0, -8)	(-1, -8)	(-3, -1)	(-3, -1)	0.39±13.50	5.00±0.37
G287.814-00.816	1.65±0.25	2.96±0.25	7.71±0.26	9.12±0.27	(1, 4)	(-1, 2)	(-1, 2)	(-1, 2)	3.53±1.99	0.42±7.32
G300.958+00.902	3.14±0.26	3.20±0.28	4.39±0.27	3.22±0.28	(3, -5)	(7, 3)	(8, 3)	(6, 1)	5.62±1.21	6.00±0.79
G300.960-00.702	<1.38	<1.38	<1.38	<1.38
G300.968+01.145	5.11±0.24	5.83±0.26	12.62±0.26	16.05±0.27	(1, -1)	(0, 0)	(0, 0)	(-1, 0)	2.20±1.80	4.76±0.35
G301.991-00.704	<1.17	<1.17	<1.17	<1.17
G302.018-00.113	<1.20	0.97±0.23	1.78±0.24	<1.20	...	(-5, -6)	(-3, 9)	...	10.14±1.40	6.53±1.59
G302.021+00.251	2.31±0.24	3.16±0.25	4.37±0.26	5.22±0.27	(-2, 0)	(-2, 0)	(-2, 0)	(-2, 0)	7.54±0.75	7.36±0.60
G302.989+00.352	<1.36	1.27±0.27	1.18±0.28	<1.36	...	(-2, -1)	(-1, 0)	...	7.39±2.68	5.41±7.34
G303.000-00.446	<1.35	<1.35	1.39±0.27	<1.35	(-2, 4)	9.75±1.26
G303.932-00.688	<1.82	2.50±0.45	5.54±0.37	5.47±0.38	...	(2, -1)	(0, 0)	(1, 0)	5.26±3.95	8.56±0.52
G303.980-00.033	<2.13	<2.13	<2.13	<2.13
G303.992+00.209	<1.24	<1.24	<1.24	<1.24
G304.887+00.635	1.79±0.33	1.56±0.33	3.03±0.34	2.71±0.35	(0, -2)	(-1, -1)	(0, -2)	(-1, 2)	4.55±3.98	8.84±0.84
G305.034+00.021	<1.48	<1.48	1.99±0.29	2.61±0.30	(-4, 1)	(-8, 6)	...	6.14±2.12
G305.044+00.573	<1.39	1.15±0.29	1.71±0.31	2.43±0.28	...	(2, -6)	(2, -8)	(-5, -3)	6.71±2.87	5.21±3.73
G305.190+00.210	10.85±0.28	13.68±0.27	22.46±0.29	27.15±0.33	(-6, -2)	(-6, -2)	(-6, -2)	(-6, -2)	6.36±0.23	7.20±0.13
G305.232+00.277	13.96±0.31	10.41±0.32	13.51±0.31	12.55±0.33	(-1, -2)	(0, -3)	(-2, -6)	(-2, -7)	5.72±0.41	5.97±0.31
G305.264-00.018	12.24±0.16	9.84±0.15	13.29±0.16	15.31±0.17	(4, 7)	(4, 8)	(4, 7)	(5, 8)	4.94±0.25	6.44±0.14
G305.357+00.193	9.05±0.38	8.68±0.38	13.97±0.37	13.88±0.38	(-3, -3)	(0, 5)	(-1, 6)	(0, 6)	6.22±0.51	6.93±0.30
G305.807-00.107	4.47±0.38	3.51±0.48	4.14±0.40	4.00±0.40	(-7, -1)	(-1, 4)	(-6, -1)	(-4, -1)	9.08±1.00	7.74±0.89
G305.887+00.016	3.81±0.42	2.82±0.42	5.18±0.41	6.57±0.43	(1, 0)	(2, 1)	(1, 1)	(1, 0)	1.00±12.68	4.88±1.32
G306.033+00.034	<1.42	<1.42	2.18±0.29	<1.42	(1, -5)	6.94±1.47
G306.053-00.040	<1.62	<1.62	3.84±0.33	2.78±0.33	(-2, -3)	(-3, -1)	...	7.40±1.12
G306.989-00.512	<1.35	<1.35	<1.35	<1.35
G307.017+00.706	<1.24	<1.24	<1.24	<1.24
G308.006-00.388	<1.38	<1.38	1.47±0.28	<1.38	(3, 0)	3.66±5.05
G308.037+00.250	<1.64	<1.64	<1.64	<1.64
G308.058-00.397	4.90±0.27	4.37±0.27	9.07±0.28	6.10±0.28	(1, 0)	(1, 0)	(2, 1)	(1, 0)	2.28±2.34	7.16±0.31
G308.914+00.126	1.42±0.31	4.04±0.33	5.57±0.32	7.54±0.32	(0, -4)	(-3, -2)	(-1, -1)	(-1, -1)	4.11±1.61	4.89±0.96
G309.001-00.030	<1.35	<1.35	<1.35	<1.35
G309.014+00.208	<1.33	1.59±0.26	2.31±0.27	2.54±0.28	...	(8, 1)	(8, 0)	(6, 2)	7.01±1.82	8.89±0.88
G309.378-00.142	6.40±0.25	4.63±0.26	7.98±0.27	6.77±0.27	(0, 5)	(0, 5)	(0, 4)	(0, 4)	5.46±0.81	7.21±0.33
G310.004+00.503	3.02±0.28	1.64±0.27	2.13±0.28	2.70±0.29	(6, 2)	(5, 2)	(4, 1)	(5, 3)	5.22±2.46	5.95±1.70
G310.008-00.022	<1.38	<1.38	<1.38	<1.38
G310.013+00.387	3.85±0.33	2.78±0.33	5.55±0.34	3.40±0.34	(-1, -1)	(0, 0)	(-1, -1)	(0, 0)	2.70±3.88	7.81±0.55
G310.013+00.389	3.53±0.28	3.07±0.28	5.66±0.29	3.68±0.29	(0, -2)	(1, -3)	(0, -2)	(0, -2)	3.56±2.09	6.76±0.60
G310.880+00.004	3.27±0.35	2.40±0.35	2.60±0.33	2.03±0.43	(0, -1)	(-1, -1)	(-4, 0)	(-10, -3)	6.37±1.78	5.94±1.67
G310.988-00.957	<1.39	<1.39	<1.39	<1.39
G311.005-00.362	<1.33	<1.33	1.95±0.28	<1.33	(8, -4)	7.79±1.54
G312.006+00.178	<1.30	<1.30	<1.30	<1.30
G312.038+00.077	1.09±0.25	1.59±0.27	1.33±0.27	1.90±0.27	(-1, 2)	(2, 3)	(2, 2)	(1, 3)	5.97±2.08	5.87±3.92
G312.071+00.080	4.72±0.38	2.67±0.33	<1.66	<1.66	(-9, -3)	(-4, -5)	4.58±2.20	...
G312.992+00.172	<1.42	<1.42	<1.42	<1.42
G313.015-00.384	<1.55	<1.55	<1.55	<1.55
G313.976+00.139	<1.53	<1.53	<1.53	<1.53
G313.994-00.084	<1.57	1.95±0.33	2.35±0.34	3.68±0.34	...	(2, -2)	(2, -2)	(2, -2)	8.51±1.27	0.39±37.76
G314.219+00.271	11.04±0.32	8.51±0.32	13.67±0.31	10.22±0.33	(-1, -2)	(-1, -1)	(-1, -1)	(-1, -1)	4.31±0.70	5.01±0.36
G314.994+00.096	1.56±0.26	1.07±0.27	<1.40	<1.40	(1, 0)	(1, 0)	6.55±2.82	...
G314.995-00.073	<1.38	<1.38	<1.38	<1.38
G315.981-00.187	<1.32	0.85±0.27	1.50±0.27	2.33±0.28	...	(8, 3)	(0, 1)	(-1, 1)	6.79±4.64	7.26±2.71
G315.985-00.605	<1.36	<1.36	<1.36	<1.36
G316.139-00.504	4.25±0.29	3.37±0.31	5.55±0.31	5.73±0.31	(1, -2)	(1, 0)	(-1, 1)	(1, 0)	5.85±1.16	7.33±0.54
G316.944+00.303	1.90±0.29	3.55±0.31	5.59±0.29	6.98±0.30	(-4, 1)	(2, 1)	(-5, 1)	(-4, 1)	5.87±1.56	2.68±1.72
G316.958+00.302	1.60±0.29	3.67±0.30	5.68±0.32	6.54±0.32	(1, 1)	(8, 1)	(2, 1)	(2, 1)	6.42±1.09	3.78±1.33
G316.963+00.022	<1.41	<1.41	<1.41	<1.41
G317.106-00.015	<1.40	<1.40	<1.40	<1.40
G317.242+00.017	<1.32	<1.32	<1.32	<1.32
G317.977-00.011	<1.35	<1.35	<1.35	<1.35
G318.049+00.086	4.43±0.34	6.01±0.36	10.50±0.35	11.71±0.36	(3, 0)	(1, 0)	(1, 0)	(-1, 1)	4.43±1.07	4.85±0.56
G318.062-00.083	<1.38	<1.38	<1.38	<1.38
G318.145-00.764	<1.34	<1.34	<1.34	<1.34
G318.776-00.151	5.73±0.26	4.61±0.27	5.02±0.27	3.53±0.27	(-1, 7)	(-1, 5)	(-1, 6)	(1, 5)	5.22±0.88	5.03±0.85
G318.786-00.397	<1.53	<1.53	<1.53	<1.53
G318.916-00.284	<1.58	1.46±0.31	1.48±0.31	<1.58	...	(2, -3)	(-4, 3)	...	8.18±1.71	10.07±1.87
G318.948-00.197	9.42±0.33	7.67±0.38	8.27±0.35	8.24±0.36	(-1, 1)	(-2, 0)	(-1, 0)	(-1, 0)	3.90±1.03	4.82±0.80
G318.982+00.323	<1.33	<1.33	<1.33	<1.33
G319.033-00.422	<1.32	<1.32	<1.32	<1.32
G319.990+00.368	<1.38	<1.38	<1.38	<1.38
G320.019-00.158	<1.43	<1.43	<1.43	<1.43
G320.168+00.824	8.55±0.24	5.23±0.25	8.83±0.25	9.55±0.27	(0, 2)	(1, 1)	(4, 0)	(2, 0)	4.41±0.97	5.85±0.47

Table 4 — *Continued*

Name	Maximum Integrated Intensity [K km s ⁻¹]				Offset from Map Center ^a [9'' pixels]				FWHM [km s ⁻¹]	
	N ₂ H ⁺	HNC	HCO ⁺	HCN	N ₂ H ⁺	HNC	HCO ⁺	HCN	HNC	HCO ⁺
G320.270+00.293	<1.42	0.98±0.27	1.38±0.29	<1.42	...	(1, -1)	(6, -7)	...	2.66±8.65	7.31±2.20
G320.874-00.351	<1.34	1.38±0.27	1.39±0.32	<1.34	...	(-2, -1)	(1, -11)	...	10.54±1.09	6.39±5.77
G321.013-00.522	<1.33	2.19±0.27	3.12±0.27	2.08±0.27	...	(-1, -3)	(0, -4)	(-4, -7)	7.20±1.21	6.29±1.02
G321.024-00.699	<1.33	<1.33	<1.33	<1.33
G321.030-00.483	2.77±0.23	2.76±0.25	5.97±0.25	6.10±0.25	(1, 1)	(0, 2)	(0, 2)	(0, 2)	3.07±2.62	5.18±0.64
G321.709+00.062	2.80±0.26	3.43±0.26	4.70±0.27	3.61±0.27	(0, 3)	(0, 3)	(0, 3)	(1, 3)	1.41±4.75	5.22±0.88
G321.935-00.007	5.56±0.28	3.92±0.30	6.10±0.31	7.75±0.31	(1, 1)	(0, 1)	(2, 0)	(2, 0)	5.63±1.03	6.70±0.57
G321.988+00.312	<1.41	<1.41	<1.41	<1.41
G322.032-00.063	<1.36	<1.36	<1.36	<1.36
G322.668+00.038	1.19±0.29	2.00±0.27	2.96±0.27	2.16±0.28	(-8, -4)	(4, 5)	(7, 4)	(2, 2)	5.39±1.92	1.70±4.96
G322.932+01.393	8.93±0.33	3.57±0.37	4.48±0.34	<1.66	(0, 1)	(1, 1)	(0, 2)	...	6.89±1.05	7.85±0.77
G323.740-00.263	7.22±0.32	4.57±0.33	6.83±0.32	7.96±0.33	(1, -1)	(0, 0)	(0, -1)	(-1, 0)	5.16±1.08	6.30±0.56
G323.921+00.400	1.94±0.28	1.52±0.29	1.48±0.30	<1.41	(6, -5)	(7, -4)	(-9, -1)	...	5.59±2.62	9.83±1.28
G324.017-00.399	<1.45	1.10±0.30	1.80±0.29	1.69±0.30	...	(-2, 3)	(0, 1)	(-2, 0)	5.73±4.61	1.57±10.68
G324.922-00.570	2.95±0.32	3.72±0.33	4.65±0.31	4.99±0.33	(0, 0)	(-1, 0)	(1, 0)	(-1, 0)	7.34±0.84	5.88±0.95
G325.004-00.408	<1.31	<1.31	<1.31	<1.31
G325.030+00.051	<1.32	<1.32	<1.32	<1.32
G325.127+00.029	1.75±0.26	2.07±0.26	3.97±0.27	4.80±0.30	(1, 2)	(1, 2)	(1, 1)	(2, 3)	1.85±6.04	4.18±1.39
G326.369-00.563	<1.89	<1.89	<1.89	<1.89
G326.410+00.596	<1.31	<1.31	2.29±0.26	2.19±0.27	(-5, 0)	(0, -3)	...	9.00±0.83
G326.668-00.732	<1.32	<1.32	<1.32	<1.32
G326.794+00.386	3.48±0.25	2.49±0.26	3.47±0.27	3.53±0.26	(0, 0)	(0, 0)	(0, 0)	(0, -1)	4.38±1.96	6.03±1.01
G326.939+00.562	1.48±0.29	2.30±0.30	3.75±0.29	2.50±0.30	(0, 1)	(-3, 2)	(-7, 4)	(0, 1)	5.54±1.84	4.07±1.60
G326.987-00.030	7.72±0.32	5.24±0.31	7.01±0.32	4.72±0.31	(2, -1)	(3, -2)	(4, -2)	(0, -3)	5.03±0.90	5.10±0.74
G326.989-00.032	7.18±0.25	5.49±0.26	7.45±0.27	4.24±0.28	(4, 1)	(4, 1)	(6, 0)	(5, 0)	5.17±0.74	5.78±0.48
G326.989-00.032	7.18±0.25	5.49±0.26	7.45±0.27	4.24±0.28	(4, 1)	(4, 1)	(6, 0)	(5, 0)	5.17±0.74	5.78±0.48
G327.005-00.754	<1.53	<1.53	<1.53	<1.53
G327.054+00.037	2.52±0.41	3.24±0.44	4.90±0.46	4.22±0.40	(2, -2)	(-4, -2)	(-6, -1)	(-2, -1)	9.13±0.92	8.22±0.84
G327.135-00.262	4.64±0.57	4.03±0.46	5.75±0.51	4.88±0.47	(-10, 3)	(-6, 2)	(-9, 2)	(-6, 1)	4.75±1.99	6.70±0.98
G327.253-00.093	<1.26	<1.26	<1.26	<1.26
G327.397-00.743	1.90±0.27	1.39±0.27	2.01±0.27	1.85±0.26	(4, 0)	(1, 0)	(2, 0)	(-3, 0)	3.52±5.65	1.25±9.67
G327.574-00.851	4.25±0.33	6.74±0.37	11.11±0.33	13.96±0.34	(2, -1)	(2, -1)	(2, -1)	(2, -2)	5.58±0.74	4.12±0.61
G327.858-00.583	<1.34	1.58±0.27	2.70±0.26	1.81±0.27	...	(2, 2)	(-2, 0)	(1, 1)	1.97±7.88	7.96±0.85
G327.895+00.150	6.07±0.25	5.19±0.26	6.67±0.26	6.96±0.27	(0, 2)	(0, 2)	(0, 2)	(0, 2)	4.68±0.87	4.86±0.66
G327.937+00.511	<1.35	<1.35	<1.35	<1.35
G327.981-00.005	<1.47	<1.47	1.22±0.27	<1.47	(2, 2)	6.62±2.50
G327.994+00.376	<1.41	1.29±0.29	<1.41	<1.41	...	(4, 3)	2.57±9.33	...
G328.255-00.410	3.77±0.26	3.87±0.27	4.65±0.27	4.73±0.27	(0, -2)	(0, -2)	(0, -2)	(-1, -2)	4.30±1.28	2.06±2.46
G328.694+00.255	<1.68	<1.68	<1.68	<1.68
G328.971+00.019	<1.59	<1.59	<1.59	<1.59
G329.034-00.674	<1.35	<1.35	<1.35	<1.35
G329.036-00.198	14.26±0.29	6.93±0.29	7.55±0.30	4.15±0.30	(2, -2)	(2, -2)	(2, -2)	(3, -3)	7.02±0.45	10.73±0.23
G329.183-00.313	7.74±0.33	4.56±0.38	4.99±0.34	3.58±0.36	(0, -1)	(-2, -2)	(1, -1)	(-2, -2)	6.25±1.02	8.14±0.64
G329.370-00.337	<1.62	<1.62	<1.62	<1.62
G329.457+00.506	7.92±0.31	7.62±0.33	7.69±0.33	8.16±0.34	(-4, 1)	(-4, 1)	(-5, -1)	(-4, 0)	7.15±0.42	5.23±0.67
G329.643-00.456	<1.24	1.97±0.27	2.58±0.29	1.50±0.27	...	(-6, 3)	(-9, 6)	(5, -9)	7.90±1.20	1.84±5.36
G329.816+00.140	4.22±0.31	3.07±0.32	5.68±0.32	4.83±0.33	(-1, -1)	(-1, -1)	(-2, -1)	(-1, -1)	2.95±3.15	3.11±1.55
G330.030+01.045	5.80±0.26	3.56±0.27	5.45±0.28	3.57±0.29	(1, -1)	(3, -2)	(1, -1)	(2, -2)	4.69±1.29	7.80±0.46
G330.042-00.058	<2.32	<2.32	<2.32	<2.32
G330.042+01.059	5.05±0.29	4.85±0.32	5.42±0.31	5.04±0.31	(8, -6)	(8, -6)	(6, -6)	(9, -6)	7.22±0.63	7.20±0.58
G330.346-00.026	<1.53	<1.53	<1.53	<1.53
G330.620-00.221	<1.55	<1.55	<1.55	<1.55
G330.778+00.256	1.79±0.31	2.49±0.35	1.74±0.33	<1.58	(3, 2)	(-2, -6)	(-3, -4)	...	8.84±1.05	6.26±2.49
G330.873-00.361	10.49±0.26	11.07±0.26	21.00±0.27	16.94±0.28	(-1, -8)	(-1, -2)	(-1, -2)	(-1, -3)	6.06±0.29	6.62±0.14
G330.948-00.504	<1.33	<1.33	2.11±0.27	1.51±0.28	(7, 2)	(-4, 2)	...	8.14±1.09
G330.986+00.330	1.75±0.29	2.79±0.38	3.28±0.33	1.99±0.30	(0, -1)	(-8, -5)	(-6, 2)	(0, -2)	11.41±0.70	9.54±0.69
G330.997-00.507	<1.45	1.24±0.26	2.66±0.28	2.02±0.28	...	(-7, -1)	(4, 3)	(-6, -4)	8.69±1.57	9.12±0.78
G331.032-00.419	6.91±0.26	6.28±0.27	11.64±0.28	8.39±0.28	(0, -1)	(0, 0)	(2, -1)	(0, 0)	4.85±0.70	5.97±0.31
G331.035+00.276	<1.30	1.28±0.26	1.66±0.28	<1.30	...	(8, -1)	(2, -2)	...	4.44±3.78	8.74±1.43
G331.221+00.012	<1.39	<1.39	<1.39	<1.39
G331.230-00.420	1.39±0.28	1.95±0.32	2.22±0.27	<1.42	(-3, 3)	(-2, 3)	(-4, 1)	...	3.63±4.18	5.43±1.80
G331.333-00.338	3.19±0.25	3.73±0.26	8.28±0.26	10.01±0.27	(-5, -3)	(-5, -3)	(-5, -3)	(-5, -3)	2.44±2.37	4.43±0.59
G331.620+00.522	4.95±0.31	3.87±0.32	4.02±0.31	2.34±0.31	(-3, 1)	(-4, -2)	(-2, 0)	(-4, -1)	8.97±0.57	7.72±0.70
G331.748+00.412	<1.54	<1.54	<1.54	<1.54
G331.914-00.320	<1.51	<1.51	<1.51	<1.51
G332.003-00.129	<1.61	<1.61	<1.61	<1.61
G332.070+00.503	1.52±0.28	1.36±0.30	3.29±0.31	2.15±0.29	(5, -7)	(-2, 2)	(2, 0)	(1, 1)	4.28±4.14	6.61±1.09
G332.093-00.421	6.33±0.29	3.75±0.30	3.68±0.31	4.98±0.31	(-3, -1)	(-3, -1)	(-8, 0)	(-2, -1)	5.61±1.09	7.65±0.92
G332.190-00.047	6.37±0.29	6.84±0.31	8.61±0.32	3.96±0.30	(-5, 2)	(-7, 1)	(-6, 1)	(-7, 2)	5.72±0.60	5.94±0.49
G332.233-00.036	9.28±0.31	7.52±0.32	7.54±0.30	6.13±0.32	(-2, -2)	(-3, -3)	(8, -2)	(-2, -4)	6.02±0.51	4.66±0.74
G332.258-00.196	<1.53	<1.53	<1.53	<1.53
G332.963+00.773	6.50±0.27	6.73±0.27	7.14±0.28	8.53±0.28	(-8, -4)	(-7, -3)	(-7, -3)	(-7, -2)	4.44±0.73	5.48±0.56
G333.000-00.436	4.53±0.30	7.39±0.34	12.80±0.33	15.31±0.32	(3, -1)	(-7, -6)	(-6, -8)	(1, 0)	6.79±0.50	5.77±0.39
G333.030-00.015	2.23±0.33	3.98±0.31	2.70±0.30	4.86±0.33	(9, -8)	(1, -5)	(5, -6)	(2, -6)	5.87±1.00	6.46±1.37

Table 4 — *Continued*

Name	Maximum Integrated Intensity [K km s ⁻¹]		Offset from Map Center ^a [9'' pixels]		FWHM [km s ⁻¹]	
	N ₂ H ⁺	HNC	HCO ⁺	HCN	HNC	HCO ⁺
G333.067−00.444	13.43±0.31	9.13±0.34	11.67±0.31	10.41±0.33	(1, -1)	(0, -1)
G333.508−00.253	8.11±0.36	4.88±0.39	7.08±0.37	5.38±0.34	(-5, -6)	(7, 4)
G333.726+00.366	4.82±0.30	3.71±0.31	5.19±0.31	4.53±0.31	(1, -3)	(-1, -3)
G333.767−00.269	4.91±0.30	4.58±0.31	6.49±0.31	3.79±0.32	(-4, 2)	(-5, 2)
G334.050+00.352	3.77±0.28	3.05±0.28	3.90±0.29	2.81±0.30	(1, -2)	(1, -2)
G334.458−00.244	2.39±0.25	2.07±0.27	<1.34	<1.34	(1, -2)	(3, -5)
G334.975−00.048	<1.36	1.24±0.31	2.20±0.29	1.61±0.29	...	(8, -10)
G335.060−00.427	6.78±0.30	2.68±0.30	2.99±0.36	<1.47	(-2, 1)	(-1, 1)
G335.075−00.411	7.97±0.30	3.72±0.32	2.09±0.32	2.34±0.31	(6, -5)	(6, -6)
G335.434−00.236	3.97±0.30	2.70±0.31	2.73±0.30	<1.54	(-6, 0)	(7, -2)
G335.800+00.181	10.66±0.34	8.65±0.35	10.98±0.34	10.17±0.35	(4, -3)	(4, -2)
G335.988−00.561	<1.45	<1.45	<1.45	<1.45
G336.022−00.816	9.20±0.30	6.50±0.31	8.86±0.31	7.21±0.31	(1, -6)	(0, -5)
G336.426−00.253	7.73±0.40	5.29±0.40	7.37±0.37	6.08±0.36	(5, 1)	(-9, 1)
G336.991+00.184	<1.57	<1.57	<1.57	<1.57
G336.994−00.019	... ^b	3.50±0.31	2.72±0.34	3.44±0.33	...	(4, 2)
G337.004+00.325	2.48±0.29	1.94±0.31	5.47±0.30	5.14±0.32	(-2, -1)	(-1, -1)
G337.436−00.394	11.02±0.26	9.80±0.32	7.73±0.29	7.82±0.30	(-2, -3)	(11, -5)
G337.912−00.469	16.72±0.31	12.40±0.32	6.96±0.32	10.25±0.32	(-2, 7)	(-1, 7)
G337.994−00.136	<1.53	2.08±0.32	2.80±0.31	3.08±0.32	...	(4, -3)
G337.994+00.078	... ^b	3.64±0.32	5.42±0.30	7.69±0.30	...	(0, 1)
G337.995+00.133	2.87±0.33	3.58±0.35	<1.66	<1.66	(1, -1)	(0, -1)
G338.927+00.635	9.70±0.29	5.74±0.32	4.71±0.30	7.22±0.30	(1, -1)	(1, -1)
G339.007+00.436	<1.51	2.05±0.36	2.86±0.30	2.93±0.31	...	(10, -5)
G339.028+00.124	<1.53	<1.53	<1.53	<1.53
G339.968−00.529	4.10±0.34	4.32±0.34	9.69±0.35	7.29±0.36	(10, 0)	(5, -1)
G340.114+00.474	<2.68	<2.68	<2.68	<2.68
G342.975+02.673	<1.40	1.18±0.27	1.90±0.28	1.74±0.28	...	(-8, 5)
G343.722−00.221	3.55±0.27	1.96±0.28	2.18±0.28	2.88±0.28	(0, -2)	(1, -1)
G345.889−01.104	7.72±0.24	6.16±0.26	8.53±0.25	8.66±0.26	(3, 2)	(3, 2)
G348.236−00.976	6.42±0.24	6.32±0.25	11.04±0.25	17.08±0.26	(4, 5)	(0, -3)
G349.642−01.093	10.74±0.24	7.94±0.25	13.84±0.25	9.16±0.25	(5, -5)	(5, -5)
G350.884+00.734	<1.18	1.44±0.24	2.06±0.24	2.25±0.25	...	(1, 5)
G351.695−01.148	7.48±0.27	6.45±0.23	8.04±0.24	12.48±0.25	(-4, 10)	(-1, 6)
G352.859−00.204	3.72±0.23	4.32±0.25	5.23±0.24	7.58±0.25	(-3, 4)	(-1, 3)
G353.057+00.542	3.54±0.28	6.03±0.28	8.79±0.28	13.11±0.29	(-2, -8)	(5, 1)

Note. — Results are listed for lines with 5σ detections in the narrow (± 2.25 km s⁻¹) moment maps, but these measurements report the moments calculated in a range of (± 8.25 km s⁻¹). Not all integrated intensity measurements at 5σ results in this broader velocity range.

^a Offsets are (x,y) offsets in units of pixels, where each pixel is 9''. Offsets are relative to the targeted center of the map, which is determined differently for the different input surveys.

^b N₂H⁺ is outside the spectral coverage for sources with $V_{LSR} < -100$ km s⁻¹

Table 5
Robust (5σ) Detections of Lines

Name	N ₂ H ⁺	¹³ CS	HNC	HCO ⁺	HCN	C ₂ H	SiO	H ¹³ CO ⁺	H ¹³ CN
G263.620−00.530	1	0	1	1	1	1	0	0	0
G264.322−00.184	1	0	1	1	1	0	0	0	0
G285.259−00.049	1	0	1	1	1	1	0	0	0
G287.814−00.816	1	0	1	1	1	1	0	0	0
G300.958+00.902	1	0	1	1	1	1	0	1	0
G300.960−00.702	0	0	0	0	0	0	0	0	0
G300.968+01.145	1	0	1	1	1	1	0	1	1
G301.991−00.704	0	0	0	0	0	0	0	0	0
G302.018−00.113	0	0	1	1	0	0	0	0	0
G302.021+00.251	1	0	1	1	1	1	0	0	0
G302.989+00.352	0	0	1	1	0	0	0	0	0
G303.000−00.446	0	0	0	1	0	0	0	0	0
G303.932−00.688	0	1	1	1	1	0	0	0	0
G303.980−00.033	0	0	0	0	0	0	0	0	0
G303.992+00.209	0	0	0	0	0	0	0	0	0
G304.887+00.635	1	0	1	1	1	0	0	0	0
G305.034+00.021	0	0	0	1	1	0	0	0	0
G305.044+00.573	0	0	1	1	1	0	0	1	0
G305.190+00.210	1	1	1	1	1	1	1	1	1
G305.232+00.277	1	0	1	1	1	1	0	1	1
G305.264−00.018	1	1	1	1	1	1	0	1	1
G305.357+00.193	1	0	1	1	1	1	0	1	1
G305.807−00.107	1	0	1	1	1	0	0	1	0
G305.887+00.016	1	0	1	1	1	1	0	0	0
G306.033+00.034	0	0	0	1	0	0	0	0	0
G306.053−00.040	0	0	0	1	1	0	0	0	0
G306.989−00.512	0	0	0	0	0	0	0	0	0
G307.017+00.706	0	0	0	0	0	0	0	0	0
G308.006−00.388	0	0	0	1	0	0	0	0	0
G308.037+00.250	0	0	0	0	0	0	0	0	0
G308.058−00.397	1	0	1	1	1	1	0	1	1
G308.914+00.126	1	1	1	1	1	1	0	0	0
G309.001−00.030	0	0	0	0	0	0	0	0	0
G309.014+00.208	0	0	1	1	1	1	0	0	0
G309.378−00.142	1	0	1	1	1	1	0	1	0
G310.004+00.503	1	0	1	1	1	1	0	0	0
G310.008−00.022	0	0	0	0	0	0	0	0	0
G310.013+00.387	1	0	1	1	1	1	0	0	0
G310.013+00.389	1	0	1	1	1	1	0	1	0
G310.880+00.004	1	0	1	1	1	0	0	0	0
G310.988−00.957	0	0	0	0	0	0	0	0	0
G311.005−00.362	0	0	0	1	0	0	0	0	0
G312.006+00.178	0	0	0	0	0	0	0	0	0
G312.038+00.077	1	0	1	1	1	1	0	0	0
G312.071+00.080	1	0	1	0	0	0	0	0	0
G312.992+00.172	0	0	0	0	0	0	0	0	0
G313.015−00.384	0	0	0	0	0	0	0	0	0
G313.976+00.139	0	0	0	0	0	0	0	0	0
G313.994−00.084	0	0	1	1	1	0	0	0	0
G314.219+00.271	1	0	1	1	1	1	0	1	1
G314.994+00.096	1	0	1	0	0	0	0	0	0
G314.995−00.073	0	0	0	0	0	0	0	0	0
G315.981−00.187	0	0	1	1	1	0	0	0	0
G315.985−00.605	0	0	0	0	0	0	0	0	0
G316.139−00.504	1	0	1	1	1	1	0	1	0
G316.944+00.303	1	0	1	1	1	1	0	0	0
G316.958+00.302	1	0	1	1	1	1	0	0	0
G316.963+00.022	0	0	0	0	0	0	0	0	0
G317.106−00.015	0	0	0	0	0	0	0	0	0
G317.242+00.017	0	0	0	0	0	0	0	0	0
G317.977−00.011	0	0	0	0	0	0	0	0	0
G318.049+00.086	1	0	0	1	1	0	0	0	0
G318.062−00.083	0	0	0	0	0	0	0	0	0
G318.145−00.764	0	0	0	0	0	0	0	0	0
G318.776−00.151	1	0	1	1	1	1	0	0	0
G318.786−00.397	0	0	0	0	0	0	0	0	0
G318.916−00.284	0	0	1	1	0	0	0	0	0
G318.948−00.197	1	0	1	1	1	1	0	1	1
G318.982+00.323	0	0	0	0	0	0	0	0	0
G319.033−00.422	0	0	0	0	0	0	0	0	0
G319.990+00.368	0	0	0	0	0	0	0	0	0
G320.019−00.158	0	0	0	0	0	0	0	0	0
G320.168+00.824	1	0	1	1	1	1	0	1	0
G320.270+00.293	0	0	1	1	0	0	0	0	0
G320.874−00.351	0	0	1	1	0	0	0	0	0

Table 5 — *Continued*

Name	N ₂ H ⁺	¹³ CS	HNC	HCO ⁺	HCN	C ₂ H	SiO	H ¹³ CO ⁺	H ¹³ CN
G321.013−00.522	0	0	1	1	1	0	0	0	0
G321.024−00.699	0	0	0	0	0	0	0	0	0
G321.030−00.483	1	0	1	1	1	1	0	0	0
G321.709+00.062	1	0	1	1	1	1	0	1	0
G321.935−00.007	1	0	1	1	1	1	0	1	0
G321.988+00.312	0	0	0	0	0	0	0	0	0
G322.032−00.063	0	0	0	0	0	0	0	0	0
G322.668+00.038	1	0	1	1	1	0	0	0	0
G322.932+01.393	1	0	1	1	0	1	1	1	0
G323.740−00.263	1	0	1	1	1	1	1	1	1
G323.921+00.400	1	0	1	1	0	0	0	0	0
G324.017−00.399	0	0	1	1	1	0	0	0	0
G324.922−00.570	1	0	1	1	1	1	0	1	0
G325.004−00.408	0	0	0	0	0	0	0	0	0
G325.030+00.051	0	0	0	0	0	0	0	0	0
G325.127+00.029	1	0	1	1	1	1	0	0	0
G326.369−00.563	0	0	0	0	0	0	0	0	0
G326.410+00.596	0	0	0	1	1	0	0	0	0
G326.668−00.732	0	0	0	0	0	0	0	0	0
G326.794+00.386	1	0	1	1	1	1	0	1	0
G326.939+00.562	1	0	1	1	1	0	0	0	0
G326.987−00.030	1	0	1	1	1	1	0	0	0
G326.989−00.032	1	0	1	1	1	1	0	0	0
G326.989−00.032	1	0	1	1	1	1	0	0	0
G327.005−00.754	0	0	0	0	0	0	0	0	0
G327.054+00.037	1	0	1	1	1	0	0	1	0
G327.135−00.262	1	0	1	1	1	1	0	1	0
G327.253−00.093	0	0	0	0	0	0	0	0	0
G327.397−00.743	1	0	1	1	1	0	0	0	0
G327.574−00.851	1	0	1	1	1	1	0	0	0
G327.858−00.583	0	0	1	1	1	0	0	0	0
G327.895+00.150	1	0	1	1	1	1	0	1	1
G327.937+00.511	0	0	0	0	0	0	0	0	0
G327.981−00.005	0	0	0	1	0	0	0	0	0
G327.994+00.376	0	0	1	0	0	0	0	0	0
G328.255−00.410	1	0	1	1	1	1	0	0	0
G328.694+00.255	0	0	0	0	0	0	0	0	0
G328.971+00.019	0	0	0	0	0	0	0	0	0
G329.034−00.674	0	0	0	0	0	0	0	0	0
G329.036−00.198	1	0	1	1	1	1	1	1	1
G329.183−00.313	1	0	1	1	1	1	0	0	1
G329.370−00.337	0	0	0	0	0	0	0	0	0
G329.457+00.506	1	0	1	1	1	0	1	1	0
G329.643−00.456	0	0	1	1	1	0	0	0	0
G329.816+00.140	1	0	1	1	1	1	0	0	0
G330.030+01.045	1	0	1	1	1	0	1	1	0
G330.042−00.058	0	0	0	0	0	0	0	0	0
G330.042+01.059	1	1	1	1	1	1	1	1	0
G330.346−00.026	0	0	0	0	0	0	0	0	0
G330.620−00.221	0	0	0	0	0	0	0	0	0
G330.778+00.256	1	0	1	1	0	0	0	0	0
G330.873−00.361	1	1	1	1	1	1	1	1	1
G330.948−00.504	0	0	0	1	1	0	0	0	0
G330.986+00.330	1	0	1	1	1	0	0	0	0
G330.997−00.507	0	0	1	1	1	0	0	0	0
G331.032−00.419	1	0	1	1	1	1	0	1	0
G331.035+00.276	0	0	1	1	0	0	0	0	0
G331.221+00.012	0	0	0	0	0	0	0	0	0
G331.230−00.420	1	0	1	1	0	0	0	0	0
G331.333−00.338	1	0	1	1	1	1	0	1	0
G331.620+00.522	1	0	1	1	1	0	0	0	0
G331.748+00.412	0	0	0	0	0	0	0	0	0
G331.914−00.320	0	0	0	0	0	0	0	0	0
G332.003−00.129	0	0	0	0	0	0	0	0	0
G332.070+00.503	1	0	1	1	1	0	0	0	0
G332.093−00.421	1	0	1	1	1	1	0	1	0
G332.190−00.047	1	0	1	1	1	0	0	1	0
G332.233−00.036	1	0	1	1	1	1	0	0	0
G332.258−00.196	0	0	0	0	0	0	0	0	0
G332.963+00.773	1	0	1	1	1	1	0	1	1
G333.000−00.436	1	0	1	1	1	1	0	1	0
G333.030−00.015	1	0	1	1	1	1	1	0	0
G333.067−00.444	1	0	1	1	1	1	0	1	1
G333.508−00.253	1	0	1	1	1	1	0	1	1
G333.726+00.366	1	0	1	1	1	1	0	1	0
G333.767−00.269	1	0	1	1	1	0	0	0	0
G334.050+00.352	1	0	1	1	1	0	0	0	0

Table 5 — *Continued*

Name	N ₂ H ⁺	¹³ CS	HNC	HCO ⁺	HCN	C ₂ H	SiO	H ¹³ CO ⁺	H ¹³ CN
G334.458−00.244	1	0	1	0	0	0	0	1	0
G334.975−00.048	0	0	1	1	1	1	0	0	0
G335.060−00.427	1	0	1	1	0	1	0	1	0
G335.075−00.411	1	1	1	1	1	0	1	1	1
G335.434−00.236	1	0	1	1	0	1	1	1	0
G335.800+00.181	1	0	1	1	1	1	0	1	1
G335.988−00.561	0	0	0	0	0	0	0	0	0
G336.022−00.816	1	0	1	1	1	1	1	1	1
G336.426−00.253	1	0	1	1	1	1	0	0	1
G336.991+00.184	0	0	0	0	0	0	0	0	0
G336.994−00.019	0	0	1	1	1	1	0	0	0
G336.994−00.019	0	0	1	1	1	1	0	0	0
G337.004+00.325	1	0	1	1	1	0	0	0	0
G337.436−00.394	1	1	1	1	1	1	1	1	1
G337.912−00.469	1	1	1	1	1	1	1	1	1
G337.994+00.078	0	0	1	1	1	1	0	0	0
G337.994−00.136	0	1	1	1	1	0	0	0	0
G337.995+00.133	1	0	1	0	0	0	1	0	0
G338.927+00.635	1	0	1	1	1	1	1	0	0
G339.007+00.436	0	0	1	1	1	0	1	0	0
G339.028+00.124	0	0	0	0	0	0	0	0	0
G339.968−00.529	1	0	1	1	1	1	0	1	0
G339.968−00.529	1	0	1	1	1	1	0	1	0
G340.114+00.474	0	0	0	0	0	0	0	0	0
G342.975+02.673	0	0	1	1	1	1	0	0	0
G343.722−00.221	1	0	1	1	1	1	0	0	0
G345.889−01.104	1	0	1	1	1	1	1	1	0
G348.236−00.976	1	0	1	1	1	1	1	1	0
G349.642−01.093	1	0	1	1	1	1	0	1	0
G350.884+00.734	0	0	1	1	1	1	0	0	0
G351.695−01.148	1	0	1	1	1	1	1	1	1
G352.859−00.204	1	0	1	1	1	1	0	0	0
G353.057+00.542	1	0	1	1	1	1	0	0	0

Note. — Robust detections correspond to 5σ integrated intensity detections excluding the 3 pixels ($27''$) on the edge of each map. Detection statistics are not shown for H41 α , CH₃CN, HC₃N, ¹³C³⁴S, HC¹³CCN, HNC O 4_{1,3} or HNC O 4_{0,4}, which have no robust detections. One corresponds to a robust detection, zero indicates no robust detection.